

On the Joint Observability of Flow Fields and Particle Properties from Lagrangian Trajectories: Evidence from Neural Data Assimilation

Ke Zhou and Samuel J. Grauer*

Department of Mechanical Engineering, Pennsylvania State University

Abstract

We numerically investigate the joint observability of flow states and unknown particle properties from Lagrangian particle tracking (LPT) data. LPT offers time-resolved, volumetric measurements of particle trajectories, but experimental tracks are spatially sparse, potentially noisy, and may be further complicated by inertial transport, raising the question of whether both Eulerian fields and particle characteristics can be reliably inferred. To address this, we develop a data assimilation framework that couples an Eulerian flow representation with Lagrangian particle models, enabling the simultaneous inference of carrier fields and particle properties under the governing equations of disperse multiphase flow. Using this approach, we establish empirical existence proofs of joint observability across three representative regimes. In a turbulent boundary layer with noisy tracer tracks ($St \rightarrow 0$), flow states and *true* particle positions are jointly observable. In homogeneous isotropic turbulence seeded with inertial particles ($St \sim 1-5$), we demonstrate simultaneous recovery of flow states and particle diameters, showing the feasibility of implicit particle characterization. In a compressible, shock-dominated flow, we report the first joint reconstructions of velocity, pressure, density, and inertial particle properties (diameter and density), highlighting both the potential and certain limits of observability in supersonic regimes. Systematic sensitivity studies further reveal how seeding density, noise level, and Stokes number govern reconstruction accuracy, yielding practical guidelines for experimental design. Taken together, these results show that the scope of LPT could be broadened to multiphase and high-speed flows, in which tracer and measurement fidelity are limited.

Keywords: Data assimilation, inverse problems, Lagrangian particle tracking, Eulerian flow reconstruction, inertial particles

1 Introduction

Understanding and modeling turbulent flow in real-world systems *ideally* calls for dense, time-resolved Eulerian fields: velocity, pressure, density, and gradient tensors of the same. These fields allow one to educe coherent structures and superstructures (Schanz et al., 2018; Schröder et al., 2009; Weiss et al., 2023), quantify energy transfer and dissipation (Schneiders et al., 2017; Schröder et al., 2022), determine surface loading from pressure and shear stress (Rival & van Oudheusden, 2017; Van Gent et al., 2017b; Jux et al., 2020), analyze buoyancy-driven transport in convection (Muralidhar, 2002; Wissink & Herlina, 2023), and so forth. In principle, scale-resolving computational fluid dynamics (CFD) methods can deliver such fields, but direct numerical simulation (DNS) becomes intractable when applied to device-scale flows at realistic Reynolds numbers (Slotnick et al., 2014; Cary et al., 2021), and large-eddy simulation depends on subgrid-scale closures that require tuning for new physical regimes (Argyropoulos & Markatos, 2015; Duraisamy et al., 2019). Even in a small subdomain, accurate simulations hinge on the fidelity of boundary conditions that are often difficult to specify, such as representative upstream disturbances (Buchta et al., 2022; Johnson et al., 2023), wall heat fluxes (Roy & Blottner, 2006), or coherent structures in the inflow (Gorlé et al., 2015; Xiao & Cinnella, 2019). These boundaries are challenging to measure experimentally, and it is rare to pose forward CFD simulations in terms of empirical unsteady boundary conditions.

Experiments, by contrast, capture the true behavior of flows but yield measurements that are typically sparse, noisy, and indirectly related to the quantities of interest. Data assimilation (DA) offers a means

*Corresponding author: sgrauer@psu.edu

to combine these complementary capabilities: enforcing the governing equations via CFD methods while matching available measurements, thereby producing physically consistent reconstructions of real flows (He et al., 2025; Zaki, 2025; Zaki & Wang, 2025). In this context, Lagrangian particle tracking (LPT) (Schröder & Schanz, 2023) is an especially attractive diagnostic because it provides time-resolved, volumetric velocity information in complex configurations and at high Reynolds numbers. The data, however, are limited to particle trajectories (also known as “tracks”) that are spatially sparse, subject to localization or tracking errors, and, in some flows, whose velocities deviate from the underlying fluid velocity due to particle inertia. This leads to the central question motivating our study: Given experimentally realizable Lagrangian data, to what extent can we recover the antecedent sequence of Eulerian flow states and salient particle properties, such as their *true* positions, sizes, and densities, by supplementing the tracks with the equations of motion for the carrier and particle phases in a DA reconstruction?

1.1 Capabilities and limitations of Lagrangian particle tracking

Lagrangian particle tracking has emerged as a leading diagnostic for volumetric velocimetry in both laboratory and field environments (Schröder et al., 2024; Bristow et al., 2023; Li et al., 2024). Compared to tomographic particle image velocimetry (PIV) (Scarano, 2012), it achieves higher spatial resolution and nearly ghost-free particle fields, enabling more accurate computation of derivatives and more reliable pressure inference (Van Gent et al., 2017a). Tracks are obtained by seeding the flow with tracer particles (or by leveraging natural tracers), imaging them with one or more cameras, and reconstructing 3D particle positions before linking them in time. Multi-camera triangulation provides high-accuracy localization from overlapping views, while single-camera methods such as digital in-line holography (DIH) (Toloui & Hong, 2015; Mallery & Hong, 2019), plenoptic cameras (Fahringer et al., 2015; Hall et al., 2017), or defocusing imaging (Guo et al., 2019) enable 4D measurements in settings where optical access is limited. Recent advances, including the predictor–corrector approach of Shake-The-Box (STB) tracking (Schanz et al., 2016; Schröder et al., 2024), object-aware LPT near boundaries (Wieneke & Rockstroh, 2024), field-scale deployments in atmospheric turbulence (Bristow et al., 2023; Li et al., 2024), and multi-pulse schemes for high-speed compressible flows (Novara et al., 2019; Manovski et al., 2021), have expanded the technique’s reach. Hence, LPT is now frequently applied to flows of practical relevance.

Two challenges are especially relevant to the question of observability in LPT. The first challenge is localization and tracking error. Although present in all LPT variants, these errors are most severe for single-camera systems (i.e., based on plenoptic or DIH imaging), which suffer from strongly anisotropic uncertainties due to depth-of-focus limitations. The largest errors occur along the optical axis (Katz & Sheng, 2010; Gao et al., 2013; Zhou et al., 2023), degrading velocity estimates and, in turn, derived quantities such as vorticity and pressure. The second challenge is inertial transport. Particles with finite response times, characterized by their Stokes number $St = \tau_p / \tau_f$, where τ_p and τ_f are characteristic time scales of the particle and carrier fluid, deviate systematically from the local fluid velocity (Melling, 1997; Raffel et al., 2018). Such particles appear in varied settings, from helium-filled soap bubbles in wind tunnels (Wolf et al., 2019; Faleiros et al., 2021) to snowflakes in the atmospheric boundary layer (Li et al., 2022; Bristow et al., 2023), causing measured trajectories to diverge from the carrier-phase motion. Both effects reduce the information content of LPT data and constrain the range of flow states and particle properties that can be inferred. Ultimately, these limitations reflect the dissipative dynamics of inertial particles, weakening the correspondence between the recorded tracks and underlying velocity field (Bec, 2003).

1.2 Data assimilation and observability in Lagrangian particle tracking

Early reconstruction approaches for LPT converted Lagrangian tracks into Eulerian fields by interpolation (Malik & Dracos, 1995; Agüí & Jimenez, 1987), but these methods were limited by the particle sampling resolution and prone to amplifying noise. Modern DA methods incorporate the Navier–Stokes equations as constraints, either *hard* (ensemble Kalman filters, Deng et al., 2018; adjoint–variational methods, Gronskis et al., 2013; Foures et al., 2014; He et al., 2024) or *soft* (physics-based interpolation with B-splines, Gesemann et al., 2016; radial basis functions, Casa & Krueger, 2013; vorticity formulations, Jeon et al., 2018). By enforcing physical consistency, these methods can reconstruct velocity fields beyond the limits of interpolation per se, recovering information at scales finer than the particle-sampling Nyquist wavenumber. Machine learning variants, like those based on physics-informed neural networks (PINNs, Raissi et al., 2019), offer flexible functional representations and have been successfully applied to a broad range of flows. They are increasingly relied upon for LPT DA, including in the present study, owing to their ease of implementation, robustness in

inverse settings, and demonstrated accuracy with sparse or noisy data (Zhou et al., 2024).

Two central difficulties remain when processing LPT data, stemming from the challenges outlined above. One is localization and tracking errors, which directly limit the fidelity of reconstructed velocities; these errors can be compounded by biases inadvertently introduced during track filtering. The other is the assumption of ideal tracers, which fails when particles have inertia, creating the additional challenge of jointly inferring particle properties alongside flow fields. In other words, the particle–flow coupling must be modeled, and it is not known a priori whether carrier-phase states and particle properties are jointly observable from the track data. A related theoretical question is whether the same framework can also recover the true particle positions from noisy measurements. Although this is rarely a primary objective in LPT, since particle positions are merely a means to recover flow fields, successful recovery of the true positions from noisy data would indicate that the governing physics and the measurements jointly constrain the track geometries, highlighting the information content of Lagrangian data in turbulence. Addressing these challenges requires a DA framework that treats particle positions as the measured quantity rather than velocities, encodes the coupled carrier-phase and particle-phase dynamics, and operates directly on noisy tracks. The development and demonstration of such a framework is one focus of this work.

1.3 Present approach and investigations into joint observability

We address the observability of flow state trajectories and particle properties using a framework we term *neural-implicit particle advection* (NIPA). NIPA couples an Eulerian flow model, parameterized by coordinate neural networks (i.e., PINNs when trained with a physics loss), to individual Lagrangian particle models that embed the particle advection equation as a hard constraint. For inertial particles, their size, density, and other attributes enter the model as trainable parameters, enabling estimation of properties that determine their response times. The governing physics enter via soft constraints on the Navier–Stokes equations for the carrier phase and an extended Maxey–Riley formulation (Subramaniam & Balachandar, 2022) for the particle (or disperse) phase. By design, NIPA works directly from the raw track positions, avoiding biases from pre-filtering, and it estimates both flow states and particle properties without requiring direct observations of either.

This framework provides the means to test joint observability across a range of flow regimes and measurement conditions. Moreover, it represents an algorithmic advance in LPT DA. We investigate observability through synthetic test cases that include noisy tracks from ideal tracers in incompressible turbulence, inertial particles in the same, and inertial particles in compressible flows with shocks. In each case, we examine whether the available track data and governing equations suffice to recover the flow states and particle properties, and we study sensitivities to seeding density, noise level, and Stokes number. These results provide empirical evidence for the existence of an inverse mapping from Lagrangian measurement manifolds, whose dimensions reflect degrees of freedom in the track data, to the flows’ global attractors in state space, which capture their essential degrees of freedom. In this way, we hope to set the stage for future theoretical work on the limits of LPT-based state estimation. The remainder of this paper outlines the reconstruction methodology in § 2, describes the flow cases used for numerical testing in § 3 and the implementation details in § 4, analyzes observability of particle positions for ideal tracers in § 5, and extends this treatment to inertial particles for turbulent and compressible flow reconstruction in § 6. Lastly, in § 7, we investigate the sensitivity of reconstruction accuracy to particle inertia in the context of noisy tracks before concluding the manuscript.

2 Methodology: neural-implicit particle advection

Understanding the joint observability of flow state trajectories and particle properties from Lagrangian data requires a DA algorithm that accounts for the physics of both phases. Existing DA methods either reconstruct the flow but treat the particles as ideal tracers, neglecting particle–fluid interactions, or they infer the particle dynamics given full knowledge of the flow field (Domínguez-Vázquez et al., 2025). Neither approach is adequate to the task at hand. To remedy this shortcoming, we introduce a new framework for LPT DA, which we call *NIPA*. It features dedicated models of both the flow and the particles, which are coupled through the governing equations of disperse multiphase flow, namely, the Navier–Stokes and extended Maxey–Riley equations. By jointly optimizing flow and particle models to satisfy these equations, NIPA recovers not only time-resolved flow states but also enhanced particle trajectories and otherwise unknown particle properties. This tool thus enables the systematic evaluation of how dataset attributes (e.g., the number and spacing of

particles, data fidelity, particle inertia, and compressibility) affect reconstruction accuracy. Below, we present our framework, define the objective loss terms, and describe our flow and particle models.

2.1 Framework for data assimilation

The NIPA framework employs “neural-implicit flow states” coupled to a set of particle models, with one model per particle, to reconstruct unsteady flows from Lagrangian tracks. A schematic of the approach is shown in figure 1. The flow field is represented using one or more coordinate neural networks, which take space–time input coordinates and return flow variables at that position and time,

$$F : \mathcal{V} \times \mathcal{T} \rightarrow \mathbb{R}^{d+1}, \quad (x, t) \mapsto (\mathbf{u}, p), \quad (2.1)$$

where $x \in \mathcal{V}$ are the spatial coordinates in the flow domain \mathcal{V} , $t \in \mathcal{T}$ is a time within the measurement interval \mathcal{T} , \mathbf{u} and p are the flow velocity and pressure, respectively, and $d \in \{2, 3\}$ is the number of spatial dimensions. Additional variables can be added to the outputs of F as needed, such as density or temperature in compressible flows. When coordinate neural networks like F are trained to minimize residuals to a set of physical equations, they are deemed to be PINNs, i.e., “physics-informed neural networks.” Network architectures used in this work are described in more detail in § 2.3.

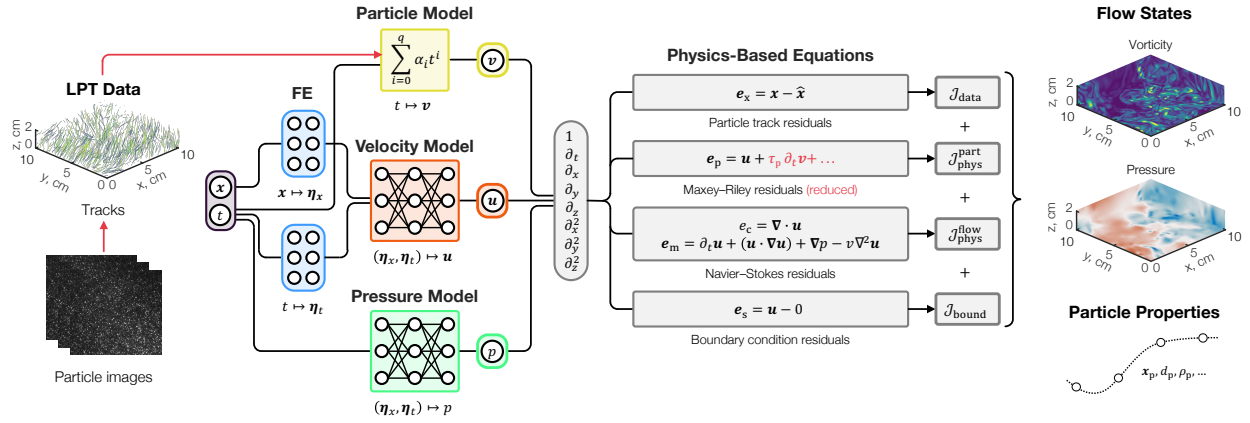


Figure 1: Neural DA solver architecture. Eulerian flow fields are represented by one or more neural networks, while each particle is modeled with a Lagrangian kinematics-constrained track (KCT) model. Flow fields, particle kinematics, and particle properties (when $St > 0$) are jointly inferred from data under the governing equations.

Measured particle tracks natively comprise sequences of spatial positions determined at the image times. Accordingly, our particle models are defined with respect to these tracked locations, which may be adjusted during training to account for localization uncertainty. For the k th particle, we introduce a dedicated model $P^{(k)}$ that represents its velocity as a continuous function of time,

$$P^{(k)} : \mathcal{T}^{(k)} \rightarrow \mathbb{R}^d, \quad t \mapsto \mathbf{v}^{(k)} \quad \text{for } k \in \{1, \dots, n_p\}, \quad (2.2)$$

where $\mathbf{v}^{(k)}$ is the velocity of particle k at time $t \in \mathcal{T}^{(k)}$, $\mathcal{T}^{(k)} \subseteq \mathcal{T}$ is the time span of that track, and n_p is the total number of particle tracks. Although $P^{(k)}$ may take various functional forms, admissible particle paths must satisfy an advection equation,

$$\mathbf{x}_j^{(k)} - \mathbf{x}_{j-1}^{(k)} = \int_{t_{j-1}}^{t_j} \mathbf{v}^{(k)}(t) dt \quad \text{for } j \in \{1, \dots, n_k - 1\} \quad (2.3)$$

where $\mathbf{x}_j^{(k)}$ is the measured position of particle k at the j th time step t_j and n_k is the number of measurement points along that track. Section 2.4 details the formulation of $P^{(k)}$, wherein the above advection equation (2.3) is enforced as a hard constraint.

Our formulation of $P^{(k)}$ provides a general framework for modeling the kinematics of both ideal tracers and inertial particles. In the latter case, properties of inertial particles like their size, density, and shape

determine τ_p and govern the particles' dynamics and coupling to the carrier fluid (Subramaniam & Balachandar, 2022). These properties, and therefore any slip velocities, are nearly always unknown in practice, complicating flow reconstruction. To address this, we treat the relevant particle properties as model parameters to be learned, enabling implicit characterization of particles from LPT data in conjunction with the equations of motion for both phases. In well-characterized experiments, by contrast, where the pertinent particle properties are known prior to reconstruction, they may be fixed in the model.

2.2 Composite objective function

Flow and particle states ought to satisfy the governing equations for both phases, they must match known boundary conditions, and they should be consistent with the observed LPT data. To achieve these objectives, the flow model F and particle models $P^{(k)}$ are trained in tandem by minimizing a composite loss,

$$\mathcal{J}_{\text{total}} = \chi_1 \mathcal{J}_{\text{data}}^x + \chi_2 \mathcal{J}_{\text{phys}}^{\text{flow}} + \chi_3 \mathcal{J}_{\text{phys}}^{\text{part}} + \chi_4 \mathcal{J}_{\text{bound}}, \quad (2.4)$$

where χ_i are weighting coefficients that balance the relative contributions of each term. The four loss terms, detailed below, are the *position-based* data fidelity term $\mathcal{J}_{\text{data}}^x$ (cf. the velocity-based term in § 2.2.4), the flow physics term $\mathcal{J}_{\text{phys}}^{\text{flow}}$, the particle physics term $\mathcal{J}_{\text{phys}}^{\text{part}}$, and the boundary condition term $\mathcal{J}_{\text{bound}}$.

2.2.1 Data fidelity loss

Particle positions are treated as trainable parameters, meaning that the estimated position of each particle at each measurement time can be adjusted during reconstruction. Without additional constraints, however, allowing the particles to move risks unmooring the models from the measurements. To anchor reconstructions, therefore, we introduce a data fidelity term that penalizes discrepancies between measured and estimated positions, weighted by the localization uncertainty,

$$\mathcal{J}_{\text{data}}^x = \left(\frac{1}{dn_p} \sum_{k=1}^{n_p} \frac{1}{n_k} \sum_{i=1}^{n_k} \left\| \mathbf{x}_i^{(k)} - \widehat{\mathbf{x}}_i^{(k)} \right\|_{\mathbf{L}}^2 - 1 \right)^2. \quad (2.5)$$

Here, $\mathbf{x}_i^{(k)}$ and $\widehat{\mathbf{x}}_i^{(k)}$ are the measured and estimated (trainable) positions of the k th particle at time t_i , with n_p total tracks and n_k samples in the k th track. The norm is the matrix-weighted Mahalanobis norm,

$$\|\Delta \mathbf{x}\|_{\mathbf{L}}^2 = \Delta \mathbf{x}^\top \mathbf{L}^\top \mathbf{L} \Delta \mathbf{x}, \quad \text{where } \mathbf{L}^\top \mathbf{L} = \mathbf{\Gamma}^{-1}$$

and $\mathbf{\Gamma}$ is the covariance matrix of the positional uncertainty. For independent, centered Gaussian localization errors, this distance follows a chi-squared distribution with d degrees of freedom, where d is the dimension of \mathbf{x} and also the expected value of the statistic. Normalizing the chi-squared statistic by d , subtracting 1, and squaring the result, as in (2.5), encourages consistency of the distances $\|\mathbf{x}_i^{(k)} - \widehat{\mathbf{x}}_i^{(k)}\|_2$ with the expected statistics of the localization errors. Values below d are indicative of overfitting to noise, while values above d suggest underfitting. In isolation, (2.5) acts as a maximum likelihood criterion for particle positions. To demonstrate this, we train the particle models in a data-only setting, which provides a baseline for comparison. When coupled with the physics and boundary losses, however, (2.5) underpins a physics-informed particle tracking method.

2.2.2 Physics-based loss terms

The flow physics loss penalizes residuals of the carrier-phase governing equations,

$$\mathcal{J}_{\text{phys}}^{\text{flow}} = \frac{\dim(\mathbf{e}_f)^{-1}}{|\mathcal{V} \times \mathcal{T}|} \int_{\mathcal{T}} \int_{\mathcal{V}} \|\mathbf{e}_f\|_2^2 \, d\mathbf{x} \, dt, \quad (2.6)$$

where \mathbf{e}_f is the residual vector associated with the governing flow equations within $\mathcal{V} \times \mathcal{T}$. For domains with transient boundaries, the space–time domain is not the simple Cartesian product of \mathcal{V} and \mathcal{T} ; see Tang et al. (2025) for details on handling such situations. While most LPT DA algorithms are restricted to incompressible flows, the present framework can be extended to compressible configurations with minimal modification. Appendix A summarizes the governing equations used in this study, including incompressible turbulent flows and a compressible example involving a conical shock wave followed by an expansion fan.

The particle physics loss is based on residuals from an equation of motion for the disperse phase,

$$\mathcal{J}_{\text{phys}}^{\text{part}} = \frac{\dim(\mathbf{e}_p)^{-1}}{n_p} \sum_{k=1}^{n_p} \frac{1}{|\mathcal{T}^{(k)}|} \int_{\mathcal{T}^{(k)}} \|\mathbf{e}_p^{(k)}\|_2^2 dt, \quad (2.7)$$

where $\mathbf{e}_p^{(k)}$ is the residual of the k th particle’s governing equation along its trajectory. For small spherical particles with a vanishing particle Reynolds number, the dynamics are described by the Maxey–Riley equation (Maxey & Riley, 1983; Capecelatro & Wagner, 2023). The specific form adopted in this work, including its adaptation for compressible flows, is summarized in appendix B. In cases with inertial particle transport, information about particle properties is obtained through the residuals in (2.7), since the equation of motion (and therefore $\mathbf{e}_p^{(k)}$) generally depends on the flow velocity \mathbf{u} , the particle velocity $\mathbf{v}^{(k)}$, and particle characteristics such as their sizes and densities.

In many LPT experiments, the particles are carefully selected to behave as ideal tracers with negligible slip velocities. In this limit, as $St \rightarrow 0$, the residuals simplify to

$$\mathbf{e}_p^{(k)} = \mathbf{u} - \mathbf{v}^{(k)}, \quad (2.8)$$

which is a pointwise equality between the fluid and particle velocities along each trajectory.

2.2.3 Boundary condition loss

Although neural state estimation does not explicitly require boundary conditions, incorporating known constraints can improve reconstruction accuracy. In turbulent boundary layers (TBLs), for instance, enforcing a no-slip condition at the wall enhances near-wall resolution, where positional uncertainties are worsened by optical reflections and where the flow scales are smallest. This combination of large relative uncertainty and fine-scale dynamics makes boundary conditions especially valuable near walls. The no-slip boundary loss is

$$\mathcal{J}_{\text{bound}} = \frac{\dim(\mathbf{u})^{-1}}{|\mathcal{A} \times \mathcal{T}|} \int_{\mathcal{T}} \int_{\mathcal{A}} \|\mathbf{u}\|_2^2 dx dt, \quad (2.9)$$

where $\mathcal{A} \subseteq \partial\mathcal{V}$ denotes the no-slip portion of the domain boundary $\partial\mathcal{V}$. This formulation can be extended to moving-wall conditions (Tang et al., 2025), enabling inference of wall motion, or to hybrid constraints that feature multiple variables (e.g., a constant free-stream density, adiabatic walls, or known pressures at tap locations) and boundary types (Dirichlet, Neumann, Robin), depending on the pertinent physics.

2.2.4 Baseline flow-only reconstruction

To evaluate the added value of joint flow–particle reconstruction, we implement a simplified baseline that neglects the particle models and instead relies on velocity information derived from the particle tracks through an intermediate step, as is common in LPT DA (Di Leoni et al., 2023; Shin & Schröder, 2025). In this baseline, the framework reduces to a flow network F that is trained to reproduce the track-based velocities $\hat{\mathbf{v}}$ while satisfying the governing equations and boundary conditions. The corresponding loss is

$$\mathcal{J}_{\text{total}} = \chi_1 \mathcal{J}_{\text{data}}^{\mathbf{u}} + \chi_2 \mathcal{J}_{\text{phys}}^{\text{flow}} + \chi_3 \mathcal{J}_{\text{bound}}, \quad (2.10)$$

where $\mathcal{J}_{\text{data}}^{\mathbf{u}}$ enforces agreement between the reconstructed flow velocity and particle velocities inferred from the tracks. The velocity-based data fidelity term is

$$\mathcal{J}_{\text{data}}^{\mathbf{u}} = \frac{1}{n_p} \sum_{k=1}^{n_p} \frac{1}{n_k} \sum_{i=1}^{n_k} \|\mathbf{u} - \hat{\mathbf{v}}_i^{(k)}\|_2^2, \quad (2.11)$$

where \mathbf{u} is the velocity field from F and $\hat{\mathbf{v}}_i^{(k)}$ is the velocity estimate for the k th particle at time t_i . Such estimates may be obtained by differentiating the tracked positions, but finite differencing amplifies noise, so smoothing or interpolation schemes like those based on B-splines, polynomial fits, or kernel convolution are often applied. Here, we demonstrate “baseline reconstructions” using both a second-order finite difference scheme (with single-sided differences at the track ends) and a quasi-optimal B-spline filter, detailed in appendix C. While these methods can suppress noise, they also embed errors in $\mathcal{J}_{\text{data}}^{\mathbf{u}}$ through the heuristic choice of filter parameters that determine $\hat{\mathbf{v}}_i^{(k)}$. By contrast, our position-based formulation in (2.5) and the

associated particle models bypass intermediate velocity estimation. Instead, we anchor the reconstruction to the measured positions, subject only to the localization error statistics.

We wish to emphasize that this baseline is used solely as a reference. It represents the performance attainable when particle–fluid coupling and particle properties are ignored, thereby highlighting the added value of a comprehensive multiphase reconstruction strategy.

2.3 Neural flow model

The flow model consists of one or more neural networks, here denoted by F , comprising an input layer, output layer, and n_1 hidden layers,

$$\mathbf{z}^{(n_1+1)} = F(\mathbf{z}^{(0)}) = \mathbf{W}^{(n_1+1)} \left[\mathbb{L}^{(n_1)} \circ \mathbb{L}^{(n_1-1)} \circ \dots \circ \mathbb{L}^{(2)} \circ G(\mathbf{z}^{(0)}) \right] + \mathbf{b}^{(n_1+1)}, \quad (2.12a)$$

with

$$\mathbf{z}^{(l)} = \mathbb{L}^l(\mathbf{z}^{(l-1)}) = \text{swish}(\mathbf{W}^{(l)} \mathbf{z}^{(l-1)} + \mathbf{b}^{(l)}), \quad \text{for } l \in \{2, \dots, n_1\}. \quad (2.12b)$$

In this expression, $\mathbf{z}^{(l)}$ are the activations at layer l , $\mathbf{W}^{(l)}$ are the corresponding weights, and $\mathbf{b}^{(l)}$ the biases. We use the swish activation,

$$\text{swish}(z_i) = \frac{z_i \exp(z_i)}{1 + \exp(z_i)}. \quad (2.13)$$

Furthermore, to mitigate the low-frequency bias that commonly occurs in gradient-based training (Wang et al., 2021), the first hidden layer $\mathbb{L}^{(1)}$ is replaced by a Fourier encoding G (Tancik et al., 2020),

$$\mathbf{z}^{(1)} = G(\mathbf{z}^{(0)}) = \left[\sin(2\pi \mathbf{f}_1 \cdot \mathbf{z}^{(0)}), \cos(2\pi \mathbf{f}_1 \cdot \mathbf{z}^{(0)}), \dots, \sin(2\pi \mathbf{f}_{n_f} \cdot \mathbf{z}^{(0)}), \cos(2\pi \mathbf{f}_{n_f} \cdot \mathbf{z}^{(0)}) \right], \quad (2.14)$$

where \mathbf{f}_i are random frequency vectors, sampled once upon initialization and fixed during training, and n_f is the number of features. For incompressible flow represented by a single network, the input is $\mathbf{z}^{(0)} = (\mathbf{x}, t)$ and the output is $\mathbf{z}^{(n_1+1)} = (\mathbf{u}, p)$.

Two additional strategies are used to improve reconstruction accuracy. First, some flow variables (e.g., density, temperature, total energy in compressible flows) must be strictly positive. Enforcing positivity stabilizes the inverse problem, and we achieve this by reparameterizing the corresponding outputs with a softplus function,

$$\text{softplus}(z_i) = \log[1 + \exp(z_i)],$$

which smoothly maps $\mathbb{R} \rightarrow (0, \infty)$. Second, different flow variables often have distinct spectral characteristics, which can hinder the performance of a shared network. For example, in homogeneous isotropic turbulence (HIT), velocity and pressure follow $\kappa^{-5/3}$ and $\kappa^{-7/3}$ scalings, respectively (Kolmogorov, 1941; Obukhov, 1949; Corrsin, 1951). In such cases, it is advantageous to assign dedicated subnetworks, e.g., $F_u : (\mathbf{x}, t) \mapsto \mathbf{u}$ and $F_p : (\mathbf{x}, t) \mapsto p$ (Zhou et al., 2024). Both strategies are employed in this work where appropriate and noted, accordingly.

2.4 Kinematics-constrained particle model

Particles are represented by models that we term “kinematics-constrained tracks” (KCTs), which embed the advection equation (2.3) as a hard constraint. As a result, trajectories given by KCTs always integrate to the positions specified by the model parameters. Measured positions are incorporated directly into the models. When high-fidelity LPT data are available, the specified particle positions can be fixed. In cases with appreciable localization uncertainty, however, they are treated as trainable variables and refined through optimization of the position-based data fidelity term $\mathcal{J}_{\text{data}}^x$ in conjunction with the physics and boundary losses. Velocities, accelerations, and intermediate positions are determined by free parameters of the model, but these parameters are themselves unconstrained. Instead, kinematic consistency is enforced by the model formulation, rather than by explicit nonlinear restrictions in parameter space. This ensures that the model outputs meet a baseline of physical fidelity without complicating gradient-based training. Figure 2 illustrates a representative KCT. In the example, tracked positions are fixed while other model parameters are adjusted, yielding multiple velocity histories that integrate to the same set of data.

In what follows, the KCT formulation is presented for a single velocity component v , with the particle index k omitted for clarity. Extension to the full vector $\mathbf{v}^{(k)}$ is straightforward. The construction draws on the theory of functional connections (Leake et al., 2022), which provides a systematic framework for

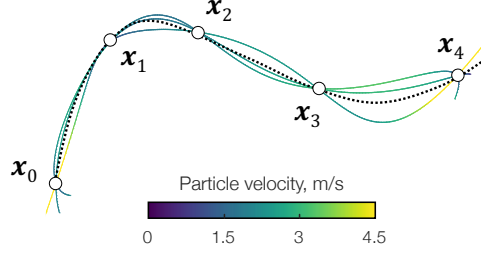


Figure 2: Illustration of a KCT (*kinematics-constrained track*) model. Colored trajectories show particle histories output by the KCT, with colors denoting particle speed. Dotted lines indicate the ground truth. Embedding (2.3) as a hard constraint ensures that tracks pass through specified particle positions (dots), regardless of velocity adjustments. Hence, the θ_i parameters are unconstrained.

converting constrained optimization problems into unconstrained ones. Within this framework, each velocity component can be written as a function of time,

$$v(t) = g(t) + \sum_{j=1}^{n_c} \eta_j \varphi_j(t), \quad (2.15)$$

where g is a user-chosen “free function,” η_j is a projection coefficient that enforces the integral constraint over the interval $[t_{j-1}, t_j]$, φ_j is a switch function that activates the projections over time, and $n_c = n_k - 1$ is the number of constraints. The choice of g determines the form of the projection coefficients. Here, g is taken as a P th-order polynomial in time,

$$g(t) = \sum_{i=0}^P \theta_i t^i, \quad (2.16)$$

with the coefficients θ_i being trainable parameters. To enforce the advection constraint in (2.3), the projection coefficients are set to

$$\eta_j = (x_j - x_{j-1}) - \int_{t_{j-1}}^{t_j} g(t) dt, \quad (2.17)$$

where x_j is the tracked position at time t_j . The switch functions are linear combinations of a set of so-called “support functions,”

$$\varphi_j(t) = \sum_{i=1}^{n_c} s_i(t) A_{ij}, \quad (2.18)$$

where s_i is the i th support function and A_{ij} is a weighting coefficient. The switch functions must successively activate the integral constraints over the corresponding intervals, which amounts to the condition

$$\int_{t_{i-1}}^{t_i} \varphi_j(t) dt = \begin{cases} 1, & i = j \\ 0, & i \neq j \end{cases} \quad \text{for } i, j \in \{1, \dots, n_c\}. \quad (2.19)$$

Enforcing this condition is equivalent to solving the linear system

$$\mathbf{S}\mathbf{A} = \mathbf{I}, \quad (2.20)$$

where \mathbf{S} is an $n_c \times n_c$ matrix with entries

$$S_{ij} = \int_{t_{i-1}}^{t_i} s_j(t) dt, \quad (2.21)$$

and \mathbf{I} is the identity matrix. The support functions s_j must yield a nonsingular matrix \mathbf{S} but are otherwise flexible. While Leake et al. (2022) suggested monomials (e.g., $s_j(t) = t^{j-1}$), the resulting KCT model becomes ill-conditioned for long tracks. Instead, we use radial basis functions,

$$s_j(t) = \exp\left[-\beta_j^2 (t - t_{0,j})^2\right], \quad (2.22)$$

with $\beta_j = (t_j - t_{j-1})^{-1}$ and where $t_{0,j} = (t_{j-1} + t_j)/2$ is the midpoint for the j th interval.

Given a set of support functions, the coefficient matrix \mathbf{A} is determined by solving (2.20), which may be done independently of the free function g and its parameters. Conversely, the projection coefficients η_j explicitly depend upon the polynomial parameters θ_i through (2.17). Substituting the polynomial form of g from (2.16) yields a closed-form expression for the projection coefficients,

$$\eta_j = (x_j - x_{j-1}) - \sum_{i=0}^P \frac{\theta_i}{i+1} (t_j^{i+1} - t_{j-1}^{i+1}), \quad (2.23)$$

where t_j^{i+1} is time t_j raised to the $(i+1)$ th power.

For ease of implementation, it is convenient to recast (2.15) in matrix form. We thus define a series of entities: a parameter vector $\boldsymbol{\theta} = \{\theta_0, \dots, \theta_P\}$, time vector $\boldsymbol{\tau}_v(t) = \{t^j \mid j = 0, \dots, P\}$, displacement vector $\boldsymbol{\delta} = \{x_j - x_{j-1} \mid j = 1, \dots, n_c\}$, support-function vector $\mathbf{s}_v(t) = \{s_j(t) \mid j = 1, \dots, n_c\}$, and $(P+1) \times n_c$ support matrix \mathbf{C} with entries

$$C_{ij} = i^{-1} (t_j^i - t_{j-1}^i). \quad (2.24)$$

Using these definitions, the KCT velocity model can be written compactly as

$$v(t) = \boldsymbol{\theta}^\top \boldsymbol{\tau}_v(t) + (\boldsymbol{\delta}^\top - \boldsymbol{\theta}^\top \mathbf{C}) \mathbf{A}^\top \mathbf{s}_v(t). \quad (2.25)$$

This representation, which is one component of P for a single particle, provides a continuous, differentiable velocity profile that inherently satisfies the advection constraint. The displacement vector $\boldsymbol{\delta}$ encodes the measured particle positions. For noisy tracks, however, the positions in $\boldsymbol{\delta}$ can be adjusted during training alongside $\boldsymbol{\theta}$, enabling refinement of particle positions at measurement times.

Integration and differentiation of the velocity model yield continuous expressions for the particle's position and acceleration. The position is

$$x(t) = \boldsymbol{\theta}^\top \boldsymbol{\tau}_x(t) + (\boldsymbol{\delta}^\top - \boldsymbol{\theta}^\top \mathbf{C}) \mathbf{A}^\top \mathbf{s}_x(t) + x_0, \quad (2.26)$$

where x_0 is the initial position of the chosen track component. The acceleration is

$$a(t) = \boldsymbol{\theta}^\top \boldsymbol{\tau}_a(t) + (\boldsymbol{\delta}^\top - \boldsymbol{\theta}^\top \mathbf{C}) \mathbf{A}^\top \mathbf{s}_a(t). \quad (2.27)$$

As in (2.25), all time dependencies are carried by the $\boldsymbol{\tau}$ and \mathbf{s} vectors. For position, these are

$$\boldsymbol{\tau}_x(t) = \left\{ t^{j+1}/(j+1) \mid j = 0, \dots, P \right\}, \quad (2.28a)$$

$$\mathbf{s}_x(t) = \left\{ \frac{\sqrt{\pi}}{2\beta_j} \operatorname{erf}[\beta_j(t - t_{0,j})] \mid j = 1, \dots, n_c \right\}, \quad (2.28b)$$

and for acceleration, they are

$$\boldsymbol{\tau}_a(t) = \left\{ j t^{j-1} \mid j = 0, \dots, P \right\}, \quad (2.28c)$$

$$\mathbf{s}_a(t) = \left\{ -2\beta_j^2(t - t_{0,j}) s_j(t) \mid j = 1, \dots, n_c \right\}. \quad (2.28d)$$

Lastly, it should be emphasized that while the KCT model enforces particle kinematics as a hard constraint, the dynamics emerge only through the joint optimization of F and $P^{(k)}$ by minimization of the loss in (2.4). For any prescribed set of positions, the KCT admits many velocity histories, as illustrated in figure 2. Accordingly, the free parameters $\boldsymbol{\theta}$ and $\boldsymbol{\delta}$ must be identified from the interplay of physics and data losses. In cases involving inertial transport with particles of unknown size, density, or other properties, the kinematic parameters alone are insufficient. Additional training variables associated with the relevant particle dynamics (diameter d_p , density ρ_p , etc.) must be included in the optimization.

3 Flow cases and datasets

We investigate the observability problem posed in the introduction through three flow configurations: a turbulent boundary layer, forced homogeneous isotropic turbulence, and supersonic flow over a cone–cylinder body. These are called the *TBL*, *HIT*, and *cone* cases, respectively. They are introduced in the order in which they are analyzed throughout the paper: tracer position observability in TBL ($St \rightarrow 0$ limit), inertial property observability in HIT and shocked flows (finite St and Re_p), and interactions between noise and inertial effects in HIT. Each dataset mimics realistic LPT conditions in terms of particle densities and accuracy. Together they incorporate standard experimental challenges, such as localization error, as well as more demanding features, including inertial transport and shocks, which are currently beyond the reach of conventional DA methods. The TBL case tests whether noisy particle tracks, when coupled with governing equations and localization uncertainty, contain enough information to jointly recover both the flow and the true particle positions. The HIT case extends this analysis to inertial particles with finite Stokes numbers, testing the joint observability of flow states, particle positions, and particle characteristics (size and density) across varying seeding densities, localization errors, and Stokes numbers. The cone case establishes joint observability in a compressible, shock-dominated flow, where inertial particles traverse an oblique shock wave followed by an expansion fan.

3.1 Turbulent boundary layer with noisy particle tracks

The first case is drawn from a DNS of channel flow with a favorable pressure gradient, obtained from the Johns Hopkins Turbulence Database (JHTDB, Perlman et al., 2007). A pressure gradient of $dp/dx = -0.0025$ drives development of TBLs along the top and bottom walls, with friction Reynolds numbers up to $Re_\tau \approx 1000$. The DNS domain spans $8\pi \times 3\pi \times 2$ and is discretized with $3072 \times 2304 \times 512$ voxels in the streamwise, spanwise, and wall-normal directions; data are stored at a dimensionless temporal resolution of 0.0065. Our study focuses on a $126 \times 54 \times 80$ -voxel subvolume near the bottom wall, corresponding to a physical region of $56 \times 12 \times 4.25 \text{ mm}^3$ (air, $\nu = 15 \text{ mm}^2/\text{s}$). In viscous units, this region spans $1546 \times 331 \times 117$ and covers the buffer layer. The viscous length and time scales are $l_\nu = 0.036 \text{ mm}$ and $\tau_\nu = 0.09 \text{ ms}$, respectively.

Synthetic LPT data are generated by advecting 70 000 ideal tracers, yielding a seeding density of 0.07 particles-per-pixel (ppp) for a 1 MP camera. Advection is performed with a fourth-order Runge–Kutta scheme and periodic boundary conditions. To mitigate boundary-related artifacts, the tracks are first computed in an extended outer domain and then cropped to an inner region that is 15% smaller in each direction. Tracks are “recorded” for 51 consecutive frames at a temporal resolution of 0.057 ms, consistent with laboratory LPT experiments (Schröder et al., 2015). The mean particle spacing is about $9l_\nu$, which is sufficient to resolve most of the flow’s energy content with PINNs (Zhou et al., 2024). The particle field is downsampled by factors of 8 and 64 to produce lower seeding density datasets with mean inter-particle spacings of $18l_\nu$ and $36l_\nu$. To mimic experimental localization errors, the ground truth positions are corrupted with additive Gaussian noise. The standard deviations are $\sigma_x = \sigma_y = 0.05N \text{ px}$ in the x – y plane, where $N \in \{1, 3, 5, 7, 9, 10\}$ indexes the noise level. In viscous units this corresponds to $0.09Nl_\nu$. Because experimental errors are often anisotropic, wall-normal noise is doubled ($\sigma_z/\sigma_x = 2$), where the z -axis is assumed to be coincident with the optical axis. The selected error range spans the performance of modern LPT techniques, including multi-camera STB (Schanz et al., 2016), plenoptic methods (Fahringer et al., 2015; Fischer et al., 2022), and DIH-LPT (Mallery & Hong, 2019). This case thus targets our initial inquiry: can noisy tracer tracks, when coupled with flow physics and localization uncertainties, provide enough information to recover both the flow fields and the *true* particle positions, i.e., indicating joint observability in the tracer limit ($St \rightarrow 0$)?

3.2 Homogeneous isotropic turbulence with bidisperse inertial particles

The second case is based on a DNS of forced incompressible HIT, also taken from the JHTDB. The flow has a Taylor microscale Reynolds number of $Re_\lambda = 433$ and is simulated in a periodic domain of size $2\pi \times 2\pi \times 2\pi$, which is discretized into 1024^3 voxels. We focus on the central 128^3 -voxel subvolume, spanning 100 frames at a dimensionless temporal resolution of 0.002. To mimic laboratory conditions, the data are dimensionalized assuming air as the carrier fluid, giving a physical volume of 10^3 cm^3 , a measurement duration of 0.032 s, and a sampling rate of 2500 Hz. The Kolmogorov length scale is $l_\eta = 350 \text{ }\mu\text{m}$ and the time scale is $\tau_\eta = 8.2 \text{ ms}$.

Particle tracks are generated by simulating 50 000 spherical soda lime glass beads with density $\rho_p = 2500 \text{ kg/m}^3$. Diameters are drawn from two Gaussian distributions: one with mean $32 \text{ }\mu\text{m}$ and

standard deviation $2\ \mu\text{m}$, the other with mean $73\ \mu\text{m}$ and standard deviation $4\ \mu\text{m}$, with equal sampling from each distribution. The particle field corresponds to a volume fraction of 3.4×10^{-6} and mass loading of 6.9×10^{-3} , near the upper boundary of the one-way coupled regime (Elghobashi, 1994; Brandt & Coletti, 2022). The resulting Stokes numbers, based on τ_η and τ_p , are approximately 1 and 5, indicating strong inertial lag and clustering (Samimy & Lele, 1991). Particle dynamics are governed by the Maxey–Riley equation (Maxey et al., 1997) with a Schiller–Naumann drag correction that is valid for $Re_p < 800$ (Schiller, 1933); here, the maximum particle Reynolds number is about 6.5 (i.e., well below 800). Following Eaton (2009) and Ling et al. (2013), the Basset history force is neglected. Trajectories are integrated with a second-order Runge–Kutta scheme, with periodic boundaries applied at the periphery of an extended domain (150 voxels). The simulation runs for 201 frames to minimize initialization and boundary artifacts.

Reconstructions are performed on the 128^3 -voxel subvolume over the final 100 frames at 0.4 ms temporal resolution. On average, 33 000 particles occupy the probe volume at any time, corresponding to 0.033 ppp for a 1 MP camera. This case provides a controlled setting to ask whether inertial particle trajectories, with finite Stokes numbers and a bidisperse size distribution, contain sufficient information to jointly recover flow states and particle properties (viz., diameters).

3.3 Supersonic cone–cylinder flow with inertial particle transport

The third case involves a steady compressible axisymmetric flow at Mach 2 over a 15° half-angle cone–cylinder body, generating an oblique shock wave at the nose and an expansion fan over the shoulder. The inflow density and temperature are $0.55\ \text{kg}/\text{m}^3$ and $166.7\ \text{K}$, and the cylinder radius is 20 mm, consistent with the experiments of Venkatakrishnan and Meier (Venkatakrishnan & Meier, 2004). The flow is simulated with the compressible, axisymmetric Navier–Stokes solver in SU2 7.3.0. The computational domain spans a radius of 0.15 m and a length of 0.25 m, with $\gamma = 1.4$. For reference, the freestream velocity is $U_\infty \approx 520\ \text{m}/\text{s}$ and the cone length is 40 mm, leading to a characteristic Reynolds number of $Re \sim 10^6$. Viscous scales for this flow are on the order of a micron in length and tens of nanoseconds in time, and the physical shock thickness is likewise sub-micron, i.e., well below both the resolution of the CFD grid or LPT experiments. Nevertheless, particle tracks throughout the domain provide physical anchors for DA reconstruction. Further details on the mesh, solver settings, and experimental validation are reported by Molnar et al. (2023).

Particle tracks are simulated for 2000 solid spherical particles, modeled as agglomerated TiO_2 spheres. Diameters are drawn from a Gaussian distribution with mean $d_p = 2\ \mu\text{m}$ and standard deviation $0.5\ \mu\text{m}$, and densities from a Gaussian distribution with mean $\rho_p = 950\ \text{kg}/\text{m}^3$ and standard deviation $100\ \text{kg}/\text{m}^3$, consistent with the measurements of Williams et al. (2015). The mean response time is $\tau_p \approx 20\ \mu\text{s}$, implying strong inertial effects through the shock and expansion. The volume fraction and mass loading are 10^{-9} and 10^{-6} , respectively, lying well within the one-way coupled regime. Particle transport is computed using a compressible drag law (see appendix B.3); particles are injected at the entrance of the computational domain at the freestream velocity and advected downstream with periodic outflow conditions. Synthetic tracks are generated for eight frames at an imaging rate of 0.5 MHz, comparable to the frame rates achieved by ultra-high-speed particle imaging systems (Beresh et al., 2020; Beresh, 2021; Manovski et al., 2021). Ultimately, this case tests whether the tracks from inertial particles crossing shocks and expansions contain enough information to jointly recover compressible flow and particle dynamics, thereby extending our assessment of observability to a shock-dominated regime.

3.4 Homogeneous isotropic turbulence with varying inertial particles and noise

Lastly, we extend the HIT case from § 3.2 to establish how localization uncertainty and inertial effects interact in determining the joint observability of flow states and particle properties. For computational efficiency, we use the central 64^3 -voxel subdomain of the HIT dataset while keeping the temporal resolution, number of frames, and advection schemes unchanged. A dense field of 6600 particles is first simulated and then downsampled by factors of 2^N , for $N \in \{1, \dots, 6\}$, producing seeding densities with inter-particle spacings from $7.3l_\eta$ to $29.3l_\eta$. The particle density is increased from $2500\ \text{kg}/\text{m}^3$ in § 3.2 to $6000\ \text{kg}/\text{m}^3$, and diameters are drawn from a Gaussian distribution with mean $33\ \mu\text{m}$ and standard deviation $4\ \mu\text{m}$. This ensures one-way coupling, even at the densest seeding condition. The mean Stokes number is $St = 3$, and no localization error is applied at this stage.

We then vary localization error and Stokes number independently. A total of 3300 particles are simulated, giving a mean spacing of $9.2l_\eta$, sufficient for a scale-resolving reconstructions in the tracer limit. Particle density is adjusted to set $St \in \{1, \dots, 5\}$ via $\rho_p = 2000St\ \text{kg}/\text{m}^3$; diameters are fixed to avoid the two-way

coupled regime. The clean tracks are corrupted with additive Gaussian noise, with $\sigma_x = \sigma_y = 0.1N$ px, assuming a 1 MP camera, and $N \in \{1, \dots, 5\}$. The lowest level ($N = 1$) corresponds to STB accuracy in ideal laboratory conditions (Schanz et al., 2016). Once again, to mimic anisotropy, wall-normal noise is doubled ($\sigma_z/\sigma_x = 2$). These settings yield 25 cases spanning a matrix of Stokes numbers and localization errors.

4 Implementation and evaluation

4.1 Neural network architectures

We implement NIPA in TensorFlow 2.10. Exact partial derivatives of the models with respect to \mathbf{x} and t are computed using automatic differentiation. Integrals over \mathcal{V} , \mathcal{A} , and \mathcal{T} in (2.6)–(2.9) are approximated by Monte Carlo sampling. We query the flow volume using a batch of 5000 points and evaluate boundary losses using 1000 points. For particle tracks, we adopt a two-stage strategy: first, 5000 tracks are sampled; second, ten random points are drawn along each track in time, yielding a batch size of 50 000 points. Although LPT data are inherently discrete, the continuous-time formulation of the KCT model enables dense temporal sampling along the tracks.

Table 1: Network architectures used for flow models (velocity, pressure, or full primitive state) across the three test cases.

Case	Flow Model	Layers \times Neurons
TBL	$F_u : (\mathbf{x}, t) \mapsto \mathbf{u}$	10×300
	$F_p : (\mathbf{x}, t) \mapsto p$	10×150
HIT	$F_u : (\mathbf{x}, t) \mapsto \mathbf{u}$	15×300
	$F_p : (\mathbf{x}, t) \mapsto p$	15×150
cone	$F : \mathbf{x} \mapsto (\rho, \mathbf{u}, T)$	10×250

The network architectures are tailored to the complexity of each flow case, with parameters listed in table 1. Flow models and submodels are denoted F , with the target field indicated in the subscript, e.g., F_u and F_p represent networks for the velocity vector and pressure fields, respectively. When no subscript is used, F maps directly to the full primitive state vector. This applies in the cone case, where $F : (\mathbf{x}, t) \mapsto (\rho, \mathbf{u}, T)$. An equation of state is incorporated into the physics loss for closure in this case, as detailed in appendix A.2. All networks employ a Fourier encoding layer, with frequency vectors f_i drawn from a standard Gaussian distribution for spatial features and from a zero-mean Gaussian with standard deviation 0.2 for temporal features. The number of Fourier features is fixed at 1024, which provides sufficient expressivity for the turbulent TBL and HIT cases.

4.2 Model initialization strategy

We next specify initialization strategies for the flow and particle models. Initialization of the flow model is straightforward: network weights are drawn from a standard normal distribution and biases are set to zero. Initialization of the kinematics-constrained particle models proceeds in three steps. First, long tracks are split into shorter segments to balance accuracy and computational cost (i.e., to keep matrix sizes manageable); guidelines for segment length are given in appendix D.1. Second, for ideal tracers, particle displacements δ are initialized directly from the raw (noisy) track data, with the polynomial coefficients in θ set to zero. We refer to this as a *cold start*, since it requires no prior information. In contrast, inertial tracks are *warm-started* using filtered track data to aid convergence. This is necessary because additional unknowns, such as particle diameters and densities, are inferred in the inertial cases, making the problem more ill-posed. Warm-started KCTs inherit both the regularity and the bias of the chosen filter, a trade-off that is necessary for stable optimization. Details of this procedure are reported in appendix D.2. Finally, all trainable parameters are normalized to order unity. This ensures that particle quantities of different units and scales across all the models can be trained together effectively using a single learning rate. Appendix D.3 details the normalization procedure and parameter selection strategy.

4.3 Training procedure

Flow and KCT models are trained together by minimizing $\mathcal{J}_{\text{total}}$. The weighting coefficients for each loss term χ_i are chosen through a simple parameter sweep. Results are relatively insensitive to modest variations in noise level or particle density once a quasi-optimal set of weights has been identified; future work will explore robust auto-weighting strategies, e.g., see Wang et al. (2021, 2022). Training is performed using the Adam optimizer, with the learning rate for flow networks fixed at 10^{-3} . For particle models, the learning rate is annealed from 10^{-4} to 10^{-5} and finally to 10^{-6} to improve precision. All cases are trained to convergence, typically requiring about 2 000 epochs per learning rate. Computations are performed on an NVIDIA RTX A6000 GPU with 48 GB of onboard memory. The total wall-clock training time is approximately 15 hours for the TBL and HIT cases and 3 hours for the cone case.

4.4 Error metrics and spectral resolution

We evaluate reconstruction accuracy using global and spectral error metrics. For a field variable φ , the normalized root-mean-square error (NRMSE) is

$$e_\varphi = \left(\frac{\langle \|\varphi - \varphi_{\text{exact}}\|_2^2 \rangle}{\langle \|\varphi_{\text{exact}}\|_2^2 \rangle} \right)^{1/2}, \quad (4.1)$$

where φ_{exact} is the ground truth. The averaging operator $\langle \cdot \rangle$ may be taken over either the spatio-temporal domain,

$$\langle \varphi \rangle_{\mathcal{V} \times \mathcal{T}} = \frac{1}{|\mathcal{V} \times \mathcal{T}|} \int_{\mathcal{T}} \int_{\mathcal{V}} \varphi(\mathbf{x}, t) \, d\mathbf{x} \, dt, \quad (4.2)$$

or across the tracks,

$$\langle \varphi \rangle_{\text{p}} = \frac{1}{n_{\text{p}}} \sum_{k=1}^{n_{\text{p}}} \frac{1}{|\mathcal{T}^{(k)}|} \int_{\mathcal{T}^{(k)}} \varphi(t) \, dt. \quad (4.3)$$

In practice, these integrals are approximated by sums over DNS grid points and time steps for flow fields, and over discrete measurement instants in $\mathcal{T}^{(k)}$ for tracks. In the unsteady flow cases, we report errors for the fluctuating component φ' , defined by a Reynolds decomposition $\varphi = \bar{\varphi} + \varphi'$. This yields a conservative estimate of reconstruction accuracy, since mean fields $\bar{\varphi}$ are generally easier to recover than turbulent fluctuations. For the steady cone flow case, errors are reported on the full fields.

Spectral error analysis quantifies accuracy across wavenumbers. The spherical averaging operator in Fourier space is

$$\langle \tilde{\varphi} \rangle_{\kappa} = \int_{\mathcal{K}(\kappa)} \tilde{\varphi}(\boldsymbol{\kappa}) \, d\boldsymbol{\kappa} \quad (4.4)$$

where $\tilde{\varphi}$ is the 3D Fourier transform of φ and $\mathcal{K}(\kappa)$ is a shell of radius κ . In practice, the integration is approximated by averaging Fourier magnitudes within discrete shells of width $\Delta\kappa$. For velocity fields, the turbulent kinetic energy (TKE) spectrum is computed using (4.4) for $\varphi = \mathbf{u} \cdot \mathbf{u}/2$. Normalized velocity error spectra are then given by

$$e_{\mathbf{u}}^2(\kappa) = \frac{\langle \|\tilde{\mathbf{u}} - \tilde{\mathbf{u}}_{\text{exact}}\|_2^2 \rangle_{\kappa}}{\langle \|\tilde{\mathbf{u}}_{\text{exact}}\|_2^2 \rangle_{\kappa}}. \quad (4.5)$$

This spectrum measures the energy of velocity reconstruction errors relative to the true turbulent energy at each wavenumber. A key reference point for interpreting these spectra is the particle sampling Nyquist wavenumber,

$$\kappa_{\text{N}} = \frac{\pi}{\bar{\delta}}, \quad (4.6)$$

where $\bar{\delta}$ is the mean inter-particle spacing. Note that κ_{N} represents the highest wavenumber resolvable from interpolation of the particle velocities, alone. In the absence of physics-based constraints, error levels beyond this limit are expected to saturate at 100%.

5 Observability of flow states with integrated particle tracking

We first examine the observability of flow states and particle positions from noisy trajectories of ideal tracers ($St \rightarrow 0$) in the incompressible TBL case. Track datasets with varying seeding densities and localization errors are generated, as described in § 3.1, to test how much information the Lagrangian data manifold contains and how effectively it can be used. We begin with track-only models: raw tracks with finite-difference velocities, filtered tracks using a quasi-optimal B-spline, and KCT tracks trained on the data loss alone. In parallel, we consider joint flow–particle reconstructions, where trajectories and flow states are optimized together. Flow accuracy is then assessed through baseline reconstructions driven by the raw and filtered tracks and compared again to the jointly-trained results. This sequence isolates the effects of track density and quality as well as the role of each constraint, i.e., data, flow physics, and particle physics.

5.1 Particle track optimization

We process datasets with three seeding densities, having mean particle spacings of $\delta = 9l_v$, $18l_v$, and $36l_v$, where l_v is the friction length, and six localization error levels, $\sigma_x = 0.09Nl_v$ for $N \in \{1, 3, 5, 7, 9, 10\}$. Four methods are used to process the tracks. First, raw tracks with velocities from finite differencing. Second, a quasi-optimal B-spline filter, described in appendix C, with supervised tuning of the segment length to minimize error across the dataset, representing a best-case scenario for B-spline filtering. Third, KCT models trained with the data loss only. These three approaches rely solely on measurement data and do not incorporate any flow physics information. Fourth, we trained KCTs jointly with the flow model, using the combined data, flow physics, and particle physics losses in the optimization, the latter of which reduces to $\mathbf{u} = \mathbf{v}$ in the tracer limit. This last setting embeds physical constraints and indicates the degree to which coupling improves track accuracy. These four datasets are labeled *raw*, *filtered*, *KCT* (meaning data only), and *joint estimation* below.

Tables 2 and 3 report error standard deviations for the x - and z -directions, respectively. Finite differencing (i.e., “raw”) amplifies positional errors into very noisy velocity and acceleration estimates; B-spline filtering, by contrast, suppresses these errors by factors of two or more, consistent with the findings of Li & Pan (2024). Data-only KCTs performs worse than raw tracks because the data loss merely promotes statistical consistency of the estimates with the presumed localization uncertainty. This makes the optimization highly ill-posed, since there are infinitely many sets of nonphysical tracks that match the target distribution. Therefore, we exclude data-only KCTs from the flow reconstructions in § 5.2.

In stark contrast, joint particle–flow estimation substantially improves the accuracy of KCT estimates, yielding lower position, velocity, and acceleration errors than filtering across all seeding densities. Unlike the first three methods, however, performance of the jointly-trained models does depend on seeding density: as density decreases, flow fields become under-resolved, which in turn degrades track accuracy. This underscores the need for sufficient Lagrangian information to achieve a converged optimization.

To highlight error trends across noise levels and seeding densities, figure 3 shows error standard deviations for the raw, filtered, and jointly estimated tracks in the x - and z -directions. At the lowest noise levels, all methods exhibit similar performance, but at high noise, joint estimation reduces velocity and acceleration errors by 40–60% compared to filtering. This improvement reflects the effect of flow physics in regularizing the track optimization, which may be regarded as *physics-informed tracking*, whereas filtering per se has a marked dependence upon heuristic parameter choices. Joint estimation also maintains high accuracy even at the sparsest case, $\delta = 36l_v$, demonstrating the stabilizing influence of physical regularization on KCT optimization. At extremely low seeding densities, however, like datasets with a handful of tracks, joint estimation is expected to deteriorate because the data are too sparse to meaningfully constrain the flow states.

Figure 4 shows a set of raw, filtered, and jointly estimated tracks at the lowest and highest noise levels for the densest seeding case, with $\delta = 9l_v$. Tracks are colored by the v_3 -component of velocity and its absolute error, where the z -direction corresponds to the optical axis and hence the largest errors. Finite-difference velocities are highly sensitive to noise, obscuring the underlying flow. Filtering suppresses this amplification and recovers tracks that qualitatively resemble the ground truth, but at high noise levels, errors in the filtered tracks remain pronounced. This is especially true within segments that exhibit high curvature, where localization errors rival the real particle motion, and near domain boundaries, where the data are sparse. Joint particle–flow estimation overcomes these challenges by enforcing physics-based constraints, yielding consistently low errors across the entire time span of each track at each noise level and each seeding density.

Table 2: Standard deviations of track errors in the x -direction under varying noise levels. Within each noise level, the three sub-rows correspond to position, velocity, and acceleration errors, normalized in turn by the friction length l_v , velocity v_v , and acceleration v_v^2/l_v . The lowest error in each row is highlighted in bold.

Noise level	Raw	Filtered	KCT	Joint estimation		
				$\delta = 9l_v$	$\delta = 18l_v$	$\delta = 36l_v$
1	0.09	0.06	0.13	0.04	0.05	0.05
	0.11	0.07	0.17	0.04	0.05	0.05
	0.14	0.05	0.30	0.05	0.05	0.05
3	0.27	0.15	0.38	0.12	0.13	0.14
	0.24	0.11	0.34	0.07	0.08	0.10
	0.32	0.08	0.35	0.06	0.07	0.08
5	0.45	0.24	0.63	0.17	0.20	0.21
	0.37	0.16	0.53	0.09	0.12	0.14
	0.50	0.10	0.65	0.08	0.09	0.09
7	0.63	0.33	0.88	0.24	0.27	0.29
	0.49	0.22	0.72	0.13	0.14	0.17
	0.67	0.12	0.82	0.09	0.09	0.10
9	0.81	0.42	1.14	0.28	0.33	0.36
	0.62	0.28	0.92	0.13	0.17	0.20
	0.84	0.14	1.20	0.09	0.10	0.11
10	0.9	0.46	1.26	0.29	0.36	0.39
	0.71	0.30	1.04	0.14	0.17	0.20
	0.97	0.14	1.29	0.09	0.10	0.11

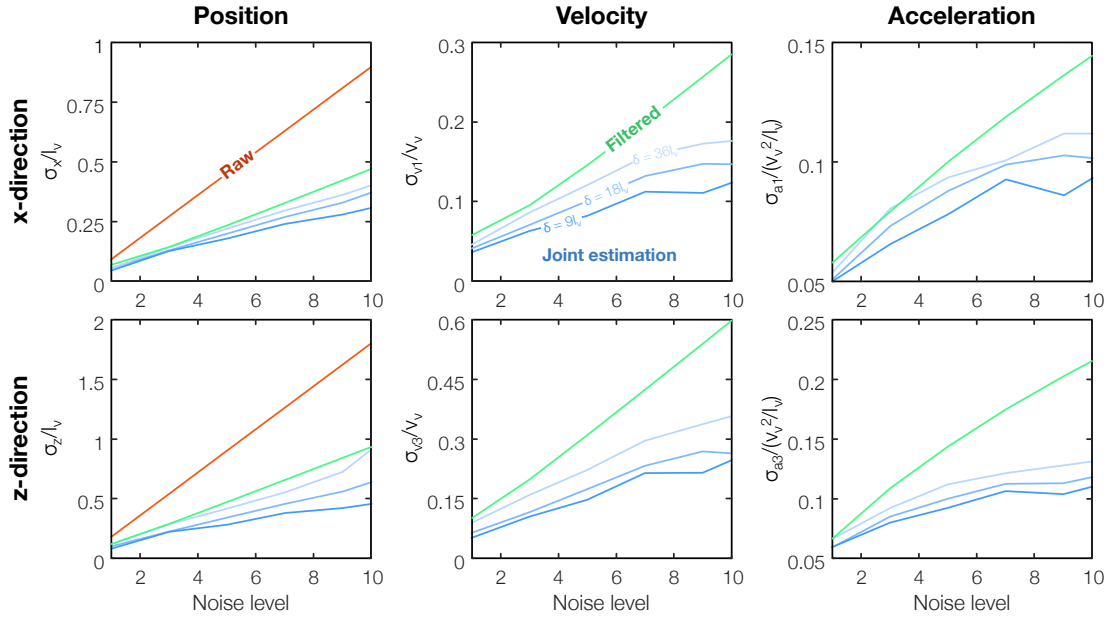


Figure 3: Standard deviations of particle position, velocity, and acceleration errors along the x - and z -axes under varying noise levels. Joint flow–particle estimation is applied at three inter-particle spacings ($\delta = 9l_v$, $18l_v$, $36l_v$). Standard deviations are normalized by viscous units. Joint estimation consistently yields the lowest errors, with some dependence on seeding density.

Table 3: Standard deviations of track errors in the z-direction under varying noise levels. Within each noise level, the three sub-rows correspond to position, velocity, and acceleration errors, normalized in turn by the friction length l_v , velocity v_v , and acceleration v_v^2/l_v . The lowest error in each row is highlighted in bold.

Noise level	Raw	Filtered	KCT	Joint estimation		
				$\delta = 9l_v$	$\delta = 18l_v$	$\delta = 36l_v$
1	0.18	0.11	0.25	0.08	0.10	0.11
	0.21	0.10	0.35	0.05	0.06	0.08
	0.28	0.06	0.52	0.06	0.06	0.07
3	0.54	0.28	0.76	0.22	0.22	0.28
	0.45	0.19	0.71	0.10	0.11	0.15
	0.63	0.11	0.82	0.07	0.09	0.10
5	0.9	0.48	1.27	0.28	0.34	0.41
	0.69	0.31	1.08	0.14	0.18	0.22
	0.96	0.15	1.19	0.09	0.10	0.11
7	1.26	0.66	1.77	0.37	0.45	0.55
	0.94	0.43	1.81	0.21	0.22	0.29
	1.3	0.17	2.42	0.10	0.11	0.12
9	1.62	0.85	2.28	0.42	0.56	0.72
	1.17	0.54	1.99	0.21	0.26	0.33
	1.67	0.20	2.80	0.10	0.11	0.13
10	1.8	0.94	2.5	0.45	0.64	0.91
	1.36	0.60	2.11	0.24	0.26	0.35
	1.87	0.22	2.85	0.11	0.12	0.13

A closeup in [figure 5](#) illustrates this difference: the jointly estimated track captures subtle fluctuations of the true trajectory, while the filtered track is visibly distorted. Quantitatively, at low noise, NRMSEs of the v_3 -component velocity are 17.6%, 8.0%, and 4.2% for finite difference, B-spline, and KCT (joint estimation), respectively; at high noise they rise to 174.4%, 64.7%, and 19.3%. Thus, noise amplifies errors in raw and filtered tracks by nearly an order of magnitude, whereas joint estimation limits the amplification to about a factor of five. This robustness carries directly into the flow reconstruction, as examined below.

5.2 Flow state reconstruction

Flow states are reconstructed by two methods. First, the baseline method, described in [§ 2.2.4](#), trains the flow model using velocities from either raw tracks (via finite differencing) or filtered tracks (via B-splines). Second, the joint estimation technique trains the KCT and flow models together using data, flow physics, and particle physics losses. [Figure 6](#) shows snapshots of the u_3 velocity and pressure fields at the lowest noise level, $\sigma_x = 0.09l_v$, based on the tracks in [figure 4](#). Flow fields are rendered on three orthogonal planes at the central snapshot. All three methods reproduce detailed flow features, but finite differencing (17.6% error) and filtering (8.0% error) yield higher track errors than the joint estimation (4.2%). Error fields confirm a progressive reduction in error from finite difference to filtering to joint estimation. The corresponding NRMSEs of u_3 are 11.6%, 9.4%, and 7.8%, while for pressure they are 14.9%, 13.4%, and 12.9%. These results highlight the feedback between particle and flow models: improved tracking both supports and is enabled by more accurate flow reconstruction.

Real LPT experiments may be subject to large localization errors, especially when using single-camera methods. [Figure 7](#) shows flow fields reconstructed at the highest noise level considered, $\sigma_x = 0.9l_v$, which is representative of high-quality plenoptic and DIH LPT. All the methods capture bulk flow structures, but baseline reconstructions computed using finite-difference velocities blur-out the finer structures and produce large velocity and pressure errors throughout the probe volume. Using velocity data from filtered tracks notably improves resolution, while joint estimation achieves the lowest errors and recovers high-frequency turbulent features. NRMSEs of the u_3 velocity are 20.9%, 15.1%, and 12.1% for finite difference, filtering, and

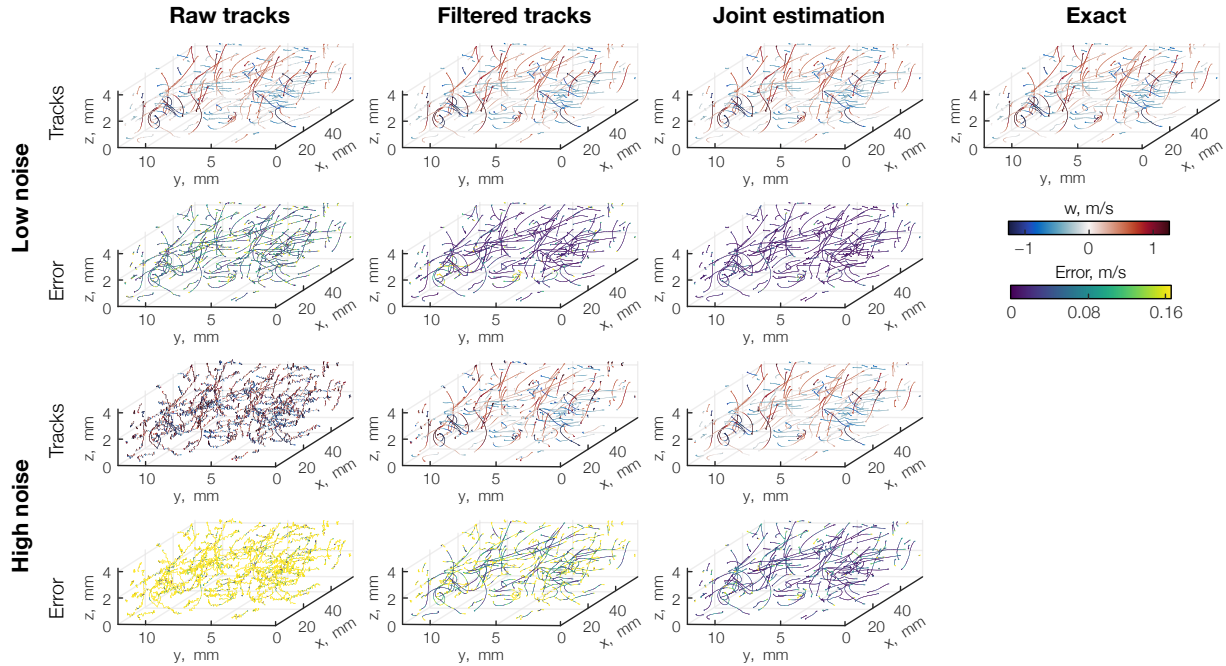


Figure 4: Comparison of exact, raw, filtered, and jointly estimated tracks and their pointwise velocity errors at the lowest ($\sigma_x = 0.09l_v$) and highest ($\sigma_x = 0.9l_v$) noise levels for the densest seeding case ($\delta = 9l_v$). Only 200 tracks are shown for visual clarity. Colors indicate the v_3 velocity or its error. Raw-track velocity errors at high noise are downscaled fivefold for visualization. Joint estimation accurately reconstructs track geometries and velocities across noise levels, while finite-difference and filtering methods show large errors, especially near boundaries and in regions of high-acceleration.

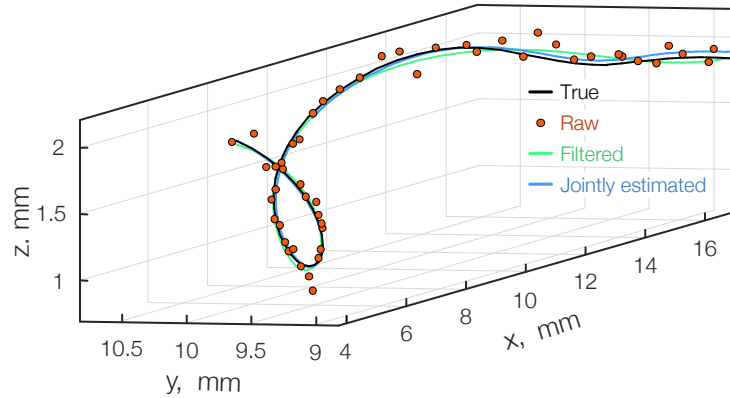


Figure 5: Close-up of a representative track under the high-noise condition. The true track is shown in black; noisy data as red dots; filtered track in green; and the jointly estimated track in blue. While filtering improves the raw data, joint estimation better recovers the true trajectory.

joint estimation, with corresponding pressure errors of 18.9%, 13.5%, and 12.2%. These results highlight the value of dynamic track models for robust flow reconstruction. The improvement is evident in the coherent structures extracted from the reconstructions: [figure 8](#) shows that while the baseline methods (using raw and filtered track velocities) yield flow fields with varying degrees of smoothing, joint estimation resolves more bona fide structures across a broad range of scales.

Estimates shown in [figures 6 to 8](#) correspond to the densest seeding, a very favorable condition, with particles spaced about 10 viscous units apart on average. To examine how seeding density and noise interact, we tested baseline and joint reconstructions across the full set of cases in [§ 3.1](#). NRMSEs of the

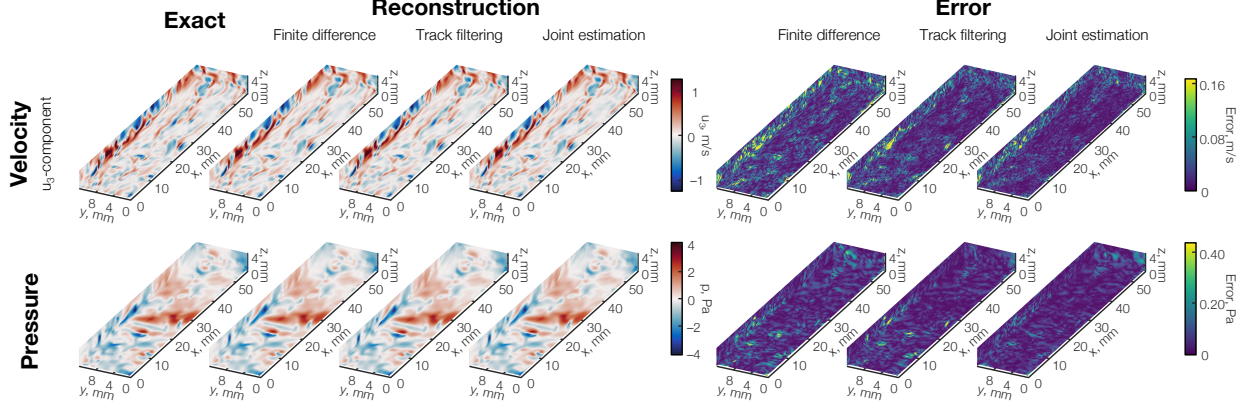


Figure 6: Exact and reconstructed flow fields (right) and absolute errors (left) at the lowest noise ($\sigma_x = 0.09l_V$) and highest seeding density ($\delta = 9l_V$). All methods recover detailed flow features, but joint estimation achieves the lowest errors.

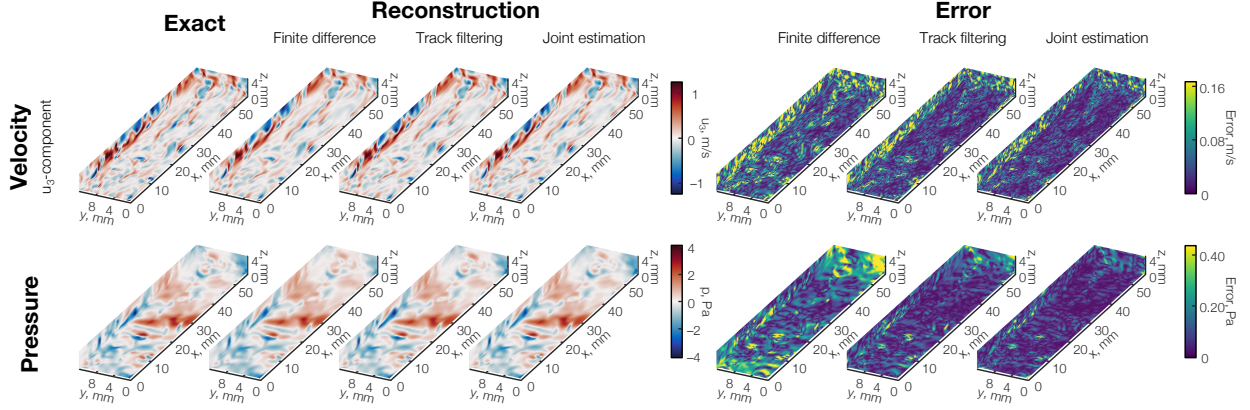


Figure 7: Exact and reconstructed flow fields (right) and absolute errors (left) at the highest noise ($\sigma_x = 0.9l_V$) and highest seeding density ($\delta = 9l_V$). Finite-difference and filtering methods blur fine features, while joint estimation robustly recovers detailed flow structures.

velocity and pressure fields are plotted in [figure 9](#) over time. As expected, larger inter-particle spacings and higher noise amplify errors for all methods. Baseline reconstructions using finite-difference velocities are especially sensitive, while those based on filtered velocities benefit from B-spline smoothing but still degrade substantially with noise. An interesting feature of the filter-based estimates is the marked inflection in error towards the beginning and end of the observation window, reflecting the fact that the filter lacks constraints on derivatives near track boundaries. In contrast, joint estimation maintains errors within a narrow band across seeding densities and noise levels, consistent with the track error trends in [figure 3](#), and provides relatively uniform accuracy over time. These results show how incorporating uncertainty information improves recovery of both particle positions and flow states, synergistically: flow physics constrains track geometry, and optimizing tracks under uncertainty yields better information for learning the flow fields. The boundary error inflections, also noted by Du et al. (2023), suggest a minimum number of timesteps is required for reliable estimation.

6 Observability of inertial particle properties in flow reconstruction

We next study the observability of flow states and inertial particle properties from particle tracks: an open question that is outside the scope of existing DA algorithms. Unlike ideal tracers, inertial particles deviate from local flow motion, reducing the dimensionality of the measurement manifold (Bec, 2003). It is therefore not obvious whether inertial track data contain sufficient information to uniquely identify both the flow states and the unknown particle properties. This amounts to a parameterized PDE-constrained inverse

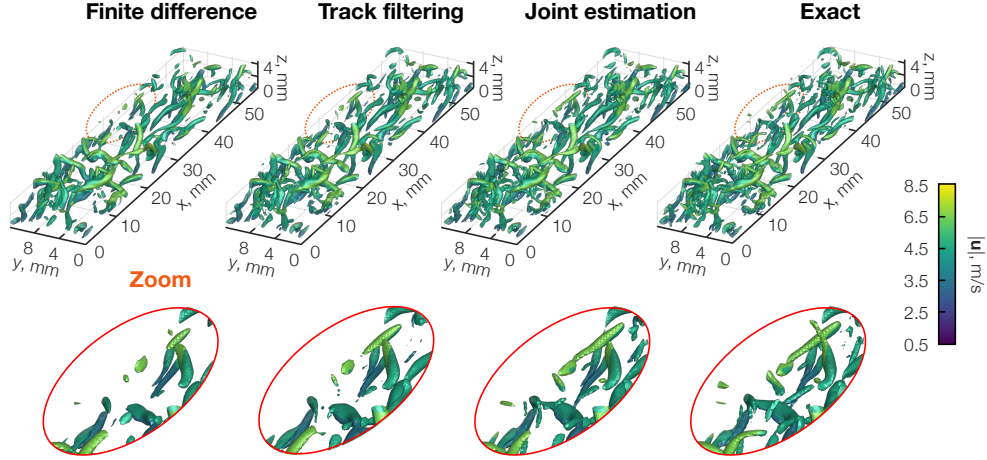


Figure 8: Coherent structures in a TBL reconstructed at the highest noise ($\sigma_x = 0.9l_v$) and densest seeding ($\delta = 9l_v$): finite difference (far left), filtered tracks (near left), joint estimation (near right), and ground truth (far right). Structures are visualized as Q -criterion isosurfaces ($Q = 2.5 \times 10^6 \text{ s}^{-2}$) colored by velocity magnitude. Joint estimation best recovers the true coherent structures.

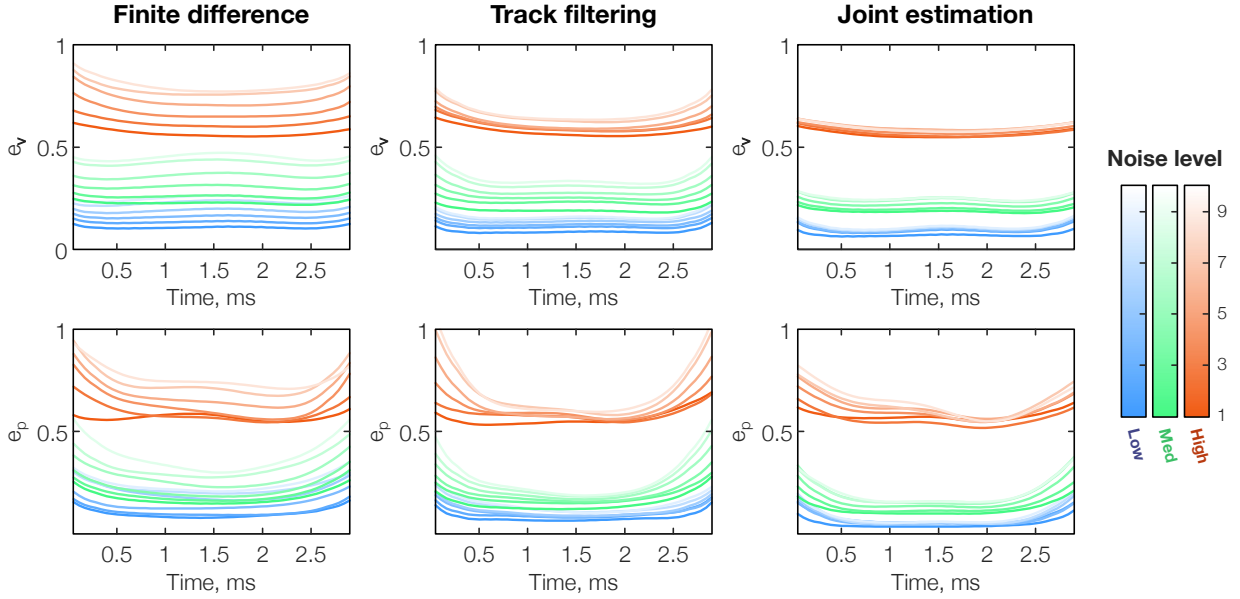


Figure 9: Velocity and pressure errors of reconstructed flows over the full time domain. Colors denote inter-particle spacings of $9l_v$ (blue), $18l_v$ (green), and $36l_v$ (red), with darker shades for lower noise and brighter for higher noise. Errors increase with both noise and spacing. Finite-difference reconstructions are most sensitive; filtering provides modest noise suppression; joint flow-particle estimation consistently maintains the low error.

problem, with the Navier–Stokes equations coupled to one parameterized Maxey–Riley equation per particle (here parameterized by particle diameter d_p and density ρ_p). The framework presented in this text allows us to empirically test the joint observability of flow states and particle properties from Lagrangian data. We show that reconstructions are in fact possible, providing an existence proof across distinct flow regimes. Two representative cases are considered: incompressible turbulence seeded with bidisperse particles governed by the Schiller–Naumann drag law (Schiller, 1933), and a supersonic, shock-dominated flow with particle motion described by the compressible Loth drag law (Loth, 2008). These examples feature one-way coupling at $St \sim 1\text{--}5$ and nontrivial compressible dynamics and shock–particle interactions in the latter case.

6.1 Homogeneous isotropic turbulence with bidisperse particles

Figure 10 shows a random subset of 3100 inertial tracks in the HIT flow, colored by particle diameter. Tracks from small and large particles are intertwined in a dense cluster, with the middle and right subplots isolating each group. The comparison highlights qualitative differences between $St \sim 1$ and $St \sim 5$ transport. Smaller particles (purple) whirl around in all directions, resembling the motion of the carrier phase, while larger particles (chartreuse) bear the clear mark of gravitational settling, drifting downward in the negative z -direction over time. Importantly, both sets of inertial tracks “mask” the underlying flow in distinct ways, and the particles are unlabeled in the reconstruction (i.e., with no knowledge of their diameter). Unlike ideal tracers, which remain strongly correlated to the flow, inertial tracks lose correlation at finite St and become effectively uncorrelated at high St . This poses a fundamental challenge for reconstructing coupled flow states and particle trajectories. Nevertheless, we show below that such reconstructions are in fact possible.

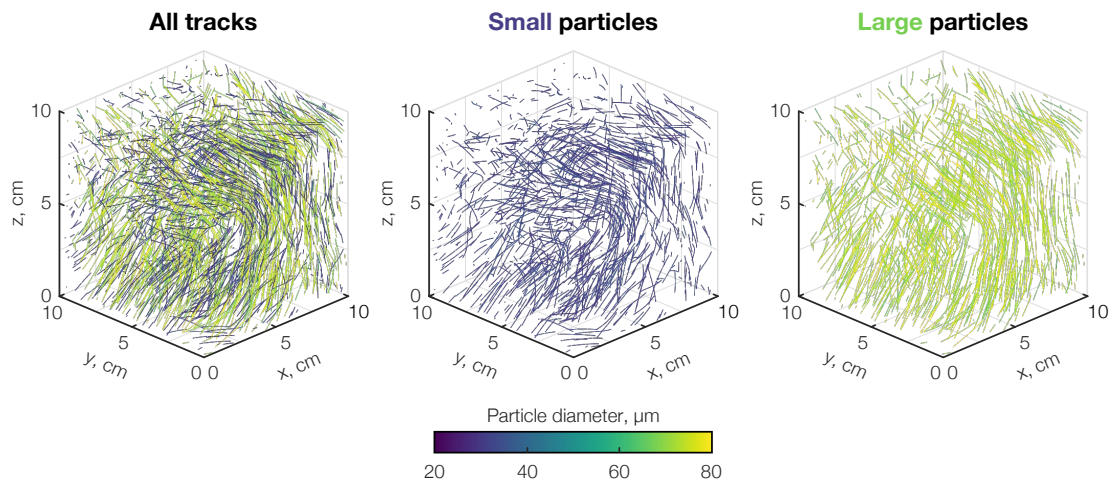


Figure 10: Random selection of bidisperse particle tracks in isotropic turbulence: (left) 3100 tracks; (middle) small particles; (right) large particles. Tracks are colored by diameter. Small particles meander in all directions equally, while larger ones are subject to pronounced gravitational settling. Tracks are unlabeled in the reconstruction (unknown d_p and hence St).

Inertial tracks from the bidisperse particles are used in both the baseline flow-only reconstruction from § 2.2.4 and the joint particle–flow reconstruction. In the baseline case, particles are treated as ideal tracers with $St \rightarrow 0$ and $\mathbf{u} = \mathbf{v}$, leading to the velocity-based data loss in (2.11). Particle velocities are obtained from the track data using the quasi-optimal B-spline filter. In the joint reconstruction, each particle diameter d_p is a trainable parameter, determining the relaxation time τ_p in the Maxey–Riley equation (B.4). For inertial particles, τ_p varies dynamically with the slip velocity through Re_p (B.1) and C_D (B.3), so the particle dynamics depend on both intrinsic particle properties and local instantaneous flow states. Our framework naturally accounts for this coupling, owing to the continuous representation of both flow and particle tracks, which necessitates joint optimization. For initialization, d_p values are drawn from a single Gaussian distribution with mean $52.5 \mu\text{m}$ and standard deviation $4 \mu\text{m}$, chosen to have minimal overlap with the true size distributions.

Figure 11 shows velocity and pressure cut plots from the ground truth DNS and both reconstructions. Cuts are taken at the bottom ($z = 0 \text{ cm}$), rear ($y = 10 \text{ cm}$), and right ($x = 10 \text{ cm}$) faces of the domain, which represent locations of high error due to the lack of boundary conditions in the reconstructions. While there is qualitative agreement between the DNS and flow-only reconstructions in the u_1 - and u_2 -components, significant errors appear in u_3 and pressure. These z -direction errors arise because the flow-only method cannot separate gravitational settling from advection, and inaccurate velocities prevent pressure recovery (Pan et al., 2016; Faiella et al., 2021; Nie et al., 2022). Even for the *apparently* accurate u_1 - and u_2 -fields, the error fields reveal large deviations. In contrast, the joint reconstructions are highly accurate across the board, as seen in the dark purple (null) error maps. Time-averaged NRMSEs are 4.2%, 3.6%, and 11.0% for the velocity components and 17.2% for pressure, compared to 18.9%, 18.3%, 92.6%, and 72.3% for the flow-only method. The reconstructions are further examined through coherent structures identified by the

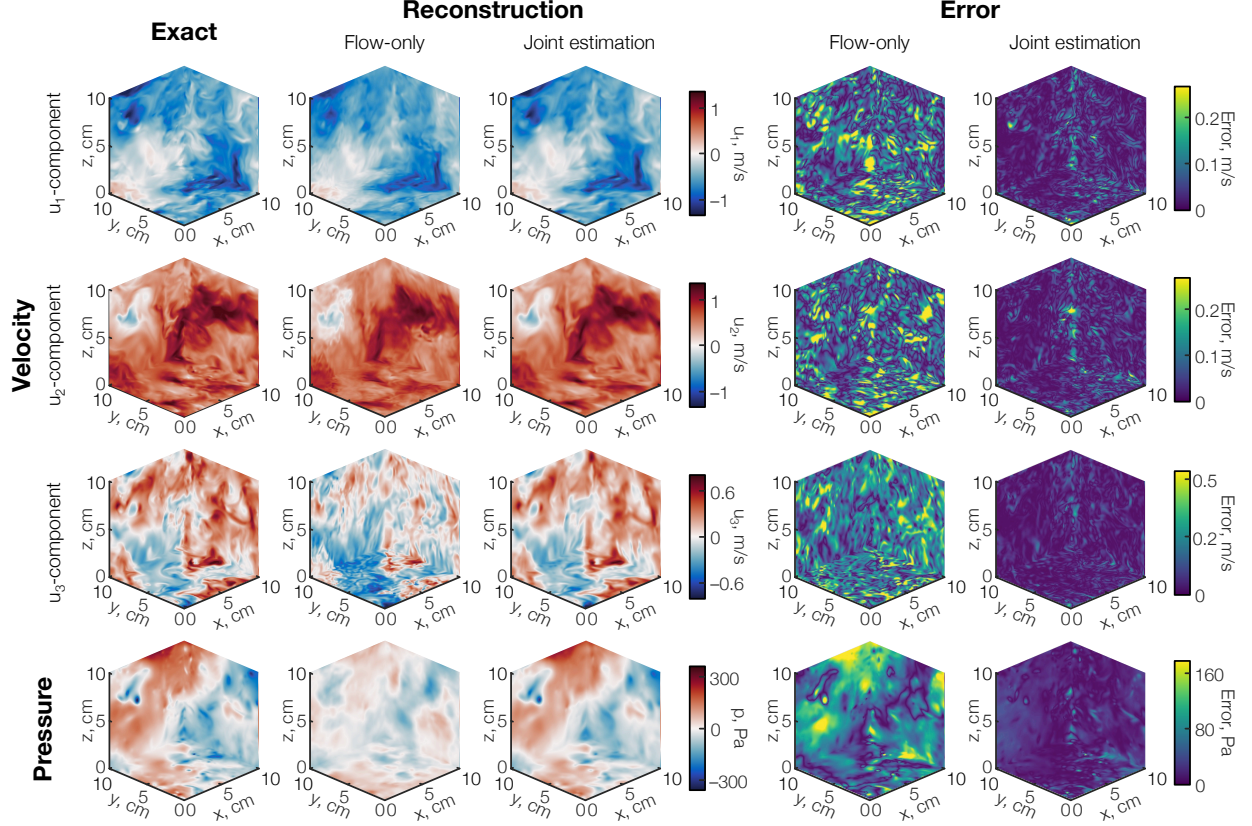


Figure 11: Isotropic turbulent flow fields: (left) exact and reconstructed velocity fields; (right) absolute errors. Accounting for particle dynamics enables accurate recovery of turbulent flow from inertial particle tracks.

Q-criterion. [Figure 12](#) shows that flow-only reconstruction produces spurious high-frequency structures, despite superficial similarity in velocity fields, while joint estimation recovers rich, physically consistent structures with only minor spatial filtering. These results establish flow observability through the veil of inertial particle dynamics.

Spectral analysis provides further insight into flow observability across scales. The left panel of [figure 13](#) compares the TKE spectra (4.4) from flow-only and joint reconstructions with the DNS reference. For context, we compute the Nyquist wavenumber κ_N of particle sampling via (4.6), which sets the maximum recoverable wavenumber for ideal tracers by interpolation alone, following the Shannon–Nyquist theorem (Jerri, 1977). Inertial particles, however, alter this picture. Flow-only reconstructions exhibit abnormal TKE behavior: underestimating energy at low wavenumbers and giving rise to spurious amplification at high wavenumbers, with low and high wavenumbers demarcated by κ_N . The low-wavenumber deficit occurs because inertial particles respond to turbulent fluctuations with a delay, collectively acting as a low-pass filter on the carrier velocity field (Mei, 1996). At high wavenumbers, weakly inertial particles ($St \sim 1$) continue to track the flow, but heavier particles ($St \sim 5$) detach from fluid parcels experiencing high acceleration such as in vortices and shear layers (Bewley et al., 2013; Voßkuhle et al., 2014). This detachment leads to multivalued velocities in an Eulerian description, which flow-only reconstructions cannot reconcile, producing spurious fluctuations at small scales.

By contrast, joint estimation reproduces the DNS spectra across wavenumbers, indicating faithful flow reconstruction. A slight underestimation of TKE appears before κ_N , consistent with the spatial filtering effect seen in [figure 12](#). This filtering reflects the additional challenge that comes with using inertial tracks, since particle properties (e.g., d_p) must be inferred simultaneously with the flow states. Because inertial particles encode only indirect information about the carrier phase, they sample the flow less efficiently than ideal tracers. In § 7.1, we show that increasing seeding density mitigates this ill-posedness and improves flow observability across wavenumbers.

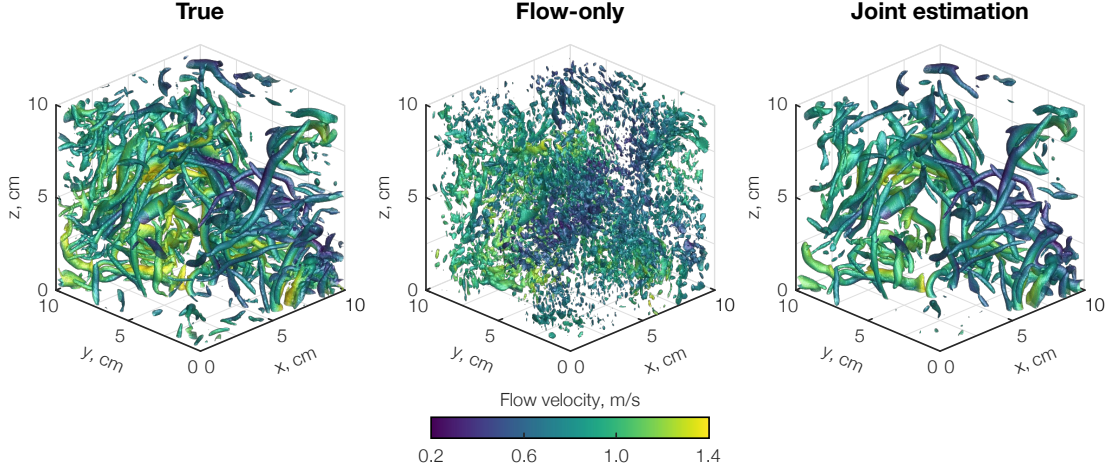


Figure 12: Coherent structures in HIT: (left) exact structures; (middle) flow-only reconstruction ($St \rightarrow 0$, $\mathbf{u} = \mathbf{v}$); (right) joint estimation with inferred St (via d_p). Structures are shown as Q -criterion isosurfaces ($Q = 5000 \text{ s}^{-2}$) colored by velocity magnitude. Flow-only reconstructions are dominated by artifacts; joint estimation recovers physically consistent structures with minor filtering.

Strictly speaking, matching the true TKE spectrum does not guarantee recovery of the target flow fields. For example, distinct snapshots of statistically stationary HIT may share the same TKE spectrum but differ in spatial structure. We therefore compute normalized velocity error spectra, defined in (4.5), and plot them in the right panel of figure 13. These spectra quantify reconstruction errors relative to TKE across wavenumbers. For reference, we also include results from ideal tracer tracks ($St \rightarrow 0$) reconstructed by two conventional methods: adaptive Gaussian windowing, a naïve interpolation approach (Agüí & Jimenez, 1987), and flow-only reconstruction. As expected, interpolation without physics asymptotes to 100% error beyond the Nyquist wavenumber, while flow-only reconstruction at the tracer limit achieves the lowest errors, particularly in the super-Nyquist region, demonstrating the ability of DA methods to recover under-resolved dynamics. By comparison, joint estimation with inertial tracks yields errors lower than naïve interpolation but higher than the tracer-based reference, confirming both the power of DA and the diminished information content of inertial tracks relative to ideal tracers. Additional inertial particles are therefore needed to establish an invertible mapping from flow trajectory in state space to the Lagrangian data manifold. Finally, flow-only reconstruction with inertial tracks performs worst in the sub-Nyquist region due to inconsistent physics assumptions, but it appears to outperform interpolation at high wavenumbers. This apparent advantage is not evidence of accurate recovery, however. It is simply a byproduct of implicit filtering by the network (low-frequency inductive bias) coinciding with the natural decay of turbulent energy at small scales.

By jointly training the inertial particle and flow models, we also recover each particle’s diameter. Figure 14 shows normalized joint probability density functions (PDFs) of the inferred and true d_p values. The left panel depicts the random initialization, drawn from a unimodal Gaussian centered between the two true size distributions. After joint estimation with flow fields, the inferred diameters separate cleanly into two clusters (middle panel), raising the Pearson correlation from 0.01 to 0.95. A slight underestimation bias is visible, with density shifted below the 45° line, which we attribute to spatial filtering in the reconstructed velocity fields: high-acceleration events are smoothed out, reducing apparent slip velocities $|\mathbf{u} - \mathbf{v}|$ and thus the inferred particle sizes. To test this, we pretrained a high-fidelity neural flow model on DNS velocity data and froze it during the particle inference. With the flow known, the estimated diameters are unbiased (right panel), and the correlation rises to 0.99. Together, these results provide an existence proof of joint observability in the inertial setting: despite the difficulty of the PDE-constrained inverse problem, both flow states and particle properties can be recovered simultaneously. They also highlight the complementary nature of flow-state and particle-property observability, whereby improving one strengthens inference of the other, echoing the results in § 5.

Before leaving this section, we emphasize that the d_p classification does not rely on prior knowledge of the flow states nor on analysis of particle images, cf. Zhang et al. (2008) and Khalitov & Longmire

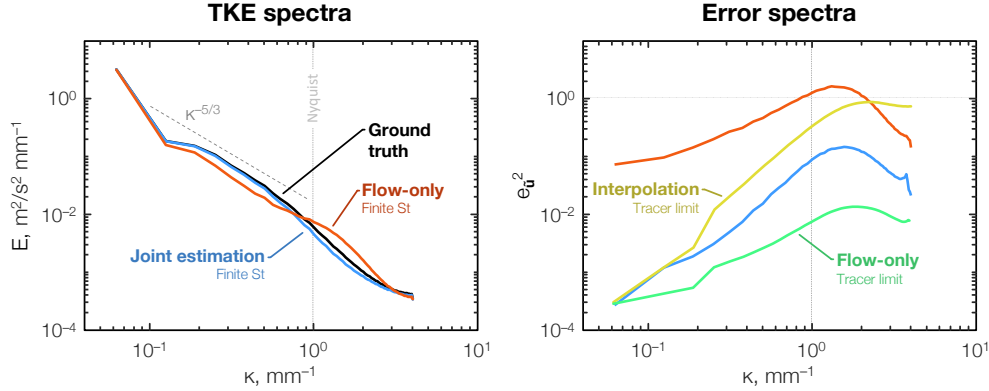


Figure 13: Comparison of TKE spectra. Left: DNS reference (black), flow-only reconstruction (red), and joint reconstruction (blue). Right: normalized error spectra relative to the true energy at each wavenumber, including errors for a flow-only reconstruction (red), joint estimation (blue), and tracer-data baselines under identical conditions: interpolation (yellow) and flow-only reconstruction (green). The Nyquist wavenumber κ_N is indicated, coinciding with peak errors. Neural reconstructions show a decay of error beyond κ_N due to the networks' inductive biases. Finite- St data yields higher errors, with the flow-only model showing a spurious peak in the super-Nyquist range caused by the $St \rightarrow 0$ assumption.

(2002). Rather, the results are obtained from the tracks and governing physics alone. When additional sizing information is available, as in Huang et al. (2021) or de la Torre & Jensen (2023), it can be incorporated into the estimation of d_p to further improve accuracy of both the flow states and particle properties. We confirmed this through supplementary tests (not shown), wherein exact values of d_p were prescribed, which yielded more accurate reconstructions of \mathbf{u} and p . Statistical priors on d_p from calibration measurements can be similarly be beneficial.

6.2 Supersonic flow over a cone-cylinder body

We next turn to joint flow-particle observability in a compressible, shock-dominated flow with inertial transport. In high-speed PIV/LPT experiments, seed particles such as TiO_2 or Al_2O_3 are subject to agglomeration due to electrostatic forces, leading to variability in the size and density of the aggregates (Williams et al., 2015). These unknown properties, combined with inertial tracks, obscure the flow field. Prior work has shown that PIV measurements of seed traversing an oblique shock wave can be used to calibrate the particle property distributions, yielding values close to manufacturer specifications (Ragni et al., 2011; Williams et al., 2015). Such calibrations can be used to assign a constant particle relaxation time, τ_p , which is then used to correct the apparent velocity fields from a cross-correlation analysis of the image pairs (Koike et al., 2007; Boiko et al., 2015). In practice, however, τ_p usually varies between particles, due to size and density differences, and along trajectories, due to local changes in temperature and viscosity. These variations introduce uncertainty into both particle properties and flow reconstructions. This challenge can be addressed via a joint reconstruction that includes trainable particle diameters and densities.

The left side of figure 15 shows simulated particle tracks colored by the local particle speed, with background shading indicating the flow speed. Regions of slip, especially in the aft-shock and expansion fan regions, are clearly visible, manifesting as streaks in the continuous flow speed field. Steep gradients in carrier-phase viscosity, density, and sound speed strongly influence particle dynamics across shocks and expansions, causing the particle response time to vary substantially throughout the domain (Williams, 2014; Williams et al., 2015). The right side of figure 15 presents PDFs of the normalized intra-track range of τ_p for particles punching through the shock wave or lurching forward in the expansion fan. Particles upstream of the shock are excluded, as they are initialized without slip and retain a constant τ_p . On average, τ_p varies by 5.5% along an eight-point track, with changes up to 40% across the shock. These variations underscore the transient character of particle relaxation in supersonic flows, a factor that is often neglected in correction schemes for high-speed PIV (Koike et al., 2007; Boiko et al., 2015).

Inertial tracks from the cone-cylinder case are pre-processed for joint estimation. Since all tracks have a uniform length of eight positions, no track splitting is required. Initial particle diameters are sampled

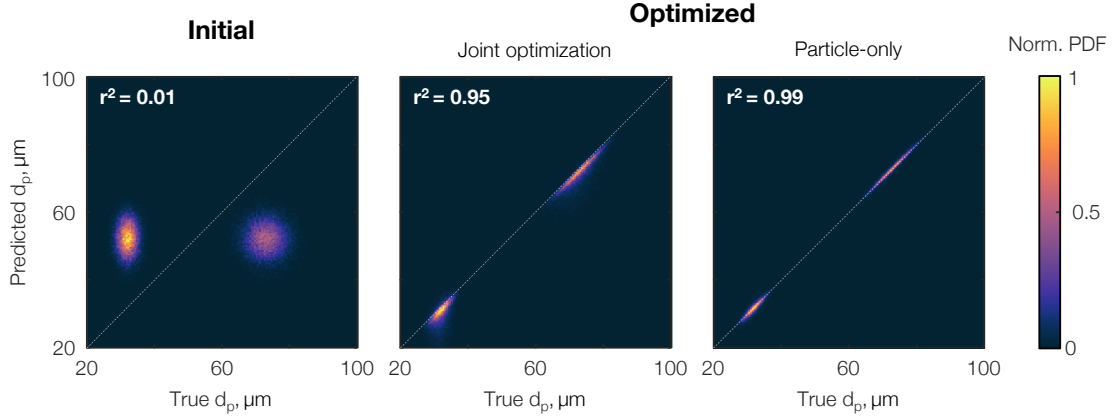


Figure 14: Normalized joint PDFs of estimated and true particle diameters: (left) initialization, (middle) estimates from joint reconstruction, (right) KCT-only estimates computed using the true velocity fields. Joint estimation recovers accurate d_p with slight underestimation due to filtered slip velocities; reconstructions with exact flow are unbiased and more accurate.

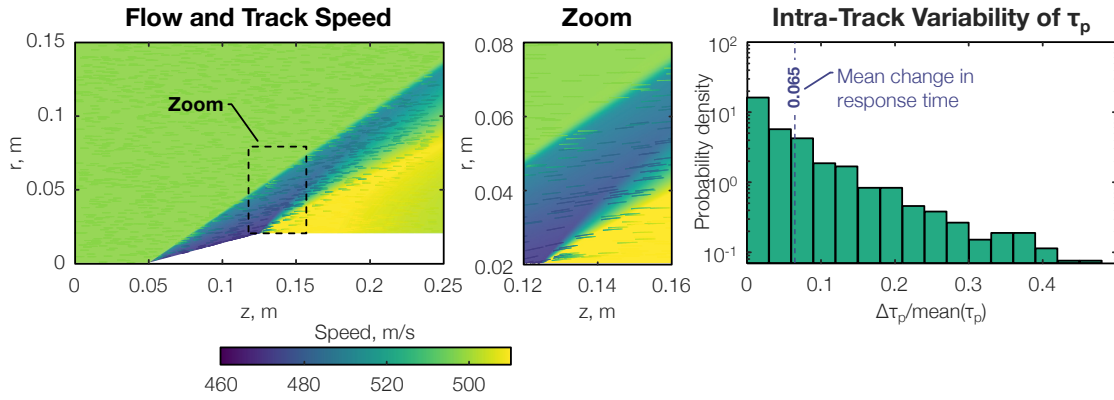


Figure 15: (left) Tracks of agglomerated TiO_2 particles in supersonic flow, colored by particle speed, overlaid on a flow speed map. Slip is visible in the aft-shock and expansion fan, manifesting as streaks. (right) PDFs of the normalized intra-track variation of τ_p , highlighting transient relaxation across shocks and expansions.

from a Gaussian distribution with mean $2 \mu\text{m}$ and standard deviation $0.5 \mu\text{m}$, while densities are drawn from a Gaussian distribution with mean 950 kg/m^3 and standard deviation 100 kg/m^3 . These distributions provide coarse estimates of particle property statistics, assumed to be available in practice from calibration experiments or manufacturer specifications. Figure 16 presents reconstructed axial and radial velocity, density, and temperature fields for the cone–cylinder flow. Results are compared against the baseline flow-only reconstruction, which assumes ideal tracers with $St \rightarrow 0$. In the baseline estimates, the shock interface is smeared and density/temperature artifacts appear near the surface, consistent with prior observations (Samimy & Lele, 1991; Ragni et al., 2011). By contrast, the joint estimation more accurately resolves both the shock structure and associated thermodynamic fields. Absolute error maps, presented on the right side of figure 16, quantify this improvement: joint estimation achieves NRMSEs of 1% (axial velocity), 6% (radial velocity), 3% (density), and 2% (temperature), compared to 2%, 25%, 18%, and 22% for the flow-only mode.

Figure 17 shows the inferred particle properties from the joint estimation in the middle column. The top row plots normalized joint PDFs of the estimated and true particle diameters. Although initialized randomly, d_p is effectively optimized to align with the ground truth, with the correlation coefficient improving from 0.01 to 0.8. As in results from the incompressible HIT case, d_p tends to be underestimated due to implicit filtering, particularly across the shock. The bottom row shows the joint PDFs of the estimated and true particle densities. In this case, the estimates diverge. This outcome is consistent with the weaker influence of density

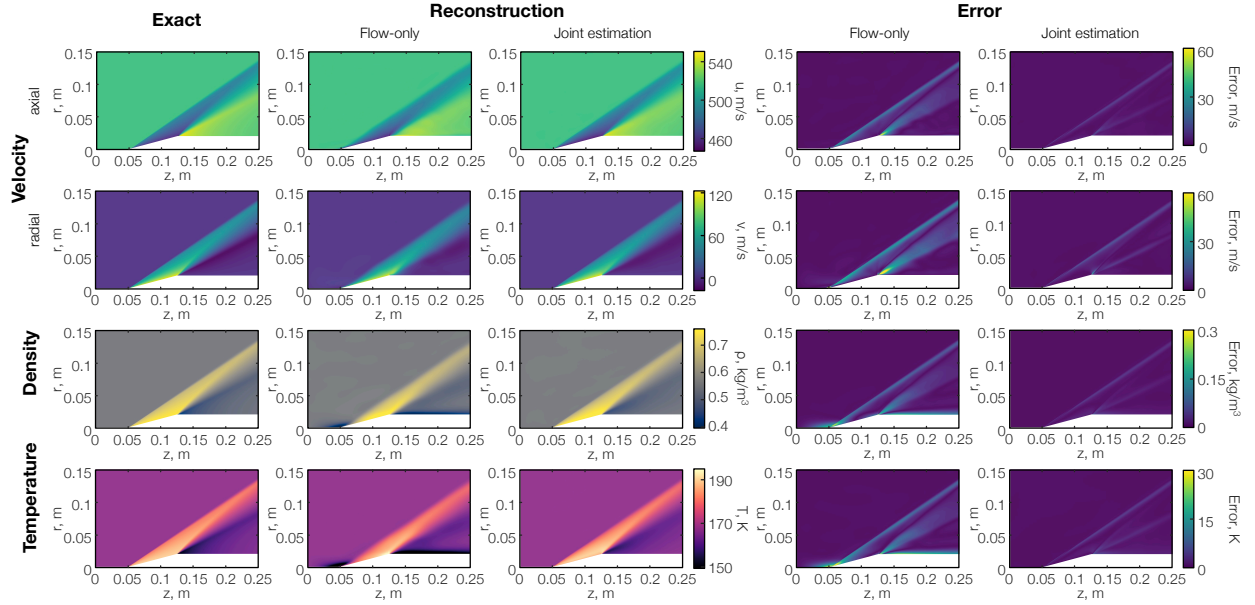


Figure 16: (left) Reconstructed cone–cylinder flow fields compared with the CFD reference. (right) Absolute error fields, showing sharper shocks and reduced artifacts with joint estimation compared to the flow-only ($St \rightarrow 0$) baseline.

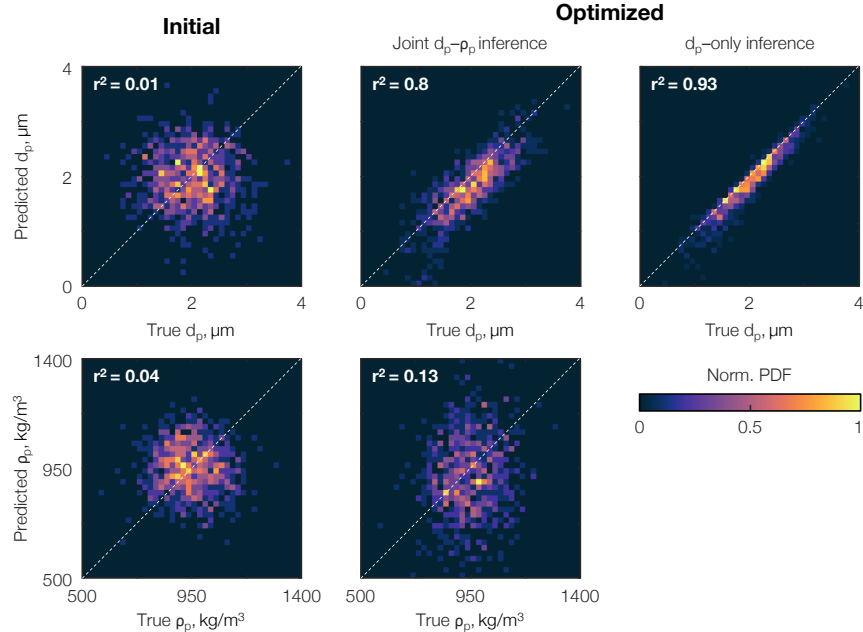


Figure 17: Implicit particle characterization in the cone–cylinder flow. Initial d_p and ρ_p (left), jointly optimized estimates (middle), and d_p -only estimates (right) compared to the ground truth values. Naturally, fixing ρ_p improves accuracy of d_p estimates.

on the response time, τ_p , which depends quadratically on d_p but only linearly on ρ_p , i.e., $\tau_p \sim \rho_p d_p^2 / C_D Re_p$ (see (B.2)). We numerically confirmed that the product of $C_D Re_p$ remains of order 0.01 for this flow, with minimal variation across particles. Importantly, even with divergent ρ_p estimates, the flow fields are reconstructed with high accuracy, as per figure 16, indicating that the flow model is relatively insensitive to uncertainties in particle density at these conditions.

The joint reconstruction above assumed both d_p and ρ_p to be unknown, representing the most challenging

scenario in supersonic PIV/LPT. To assess how prior knowledge of particle properties affects joint observability, we reduce the degrees of freedom by fixing ρ_p to its true values and allowing only d_p to vary. The resulting d_p estimates are shown on the right side of [figure 17](#). Compared to the fully unconstrained case (the middle of [figure 17](#)), the alignment between estimated and true d_p values is substantially improved, with the Pearson correlation coefficient rising from 0.8 to 0.93. This enhanced particle characterization translates directly into better flow reconstruction, lowering the NRMSEs to 0.5% (axial velocity), 4.8% (radial velocity), 2.3% (density), and 1.3% (temperature). These results underscore the complementary nature of the two phases: even partial knowledge of particle properties (here, ρ_p) improves observability of both flow and particle states. From a DA perspective, this suggests an alternative strategy for supersonic LPT. Rather than pushing toward ever-smaller tracer particles, lowering their scattering cross-section and weakening the signal, one could employ finite-size particles with carefully controlled properties (shape, size, density). Accurate knowledge of these properties reduces model ambiguity and, in turn, enhances the joint observability of disperse multiphase flows.

7 Interaction of noise and inertia in flow–particle reconstruction

Section 6 establishes the possibility of jointly observable flow states and inertial particle properties, albeit under ideal conditions with dense, noise-free track data. In real LPT experiments, one must contend with sparse and noisy tracks that could potentially obscure observability. When the number of particles is small, the inversion problem becomes ill-posed: the available data eventually become insufficient to recover both particle properties and flow states. Even when the problem remains formally well-posed, reconstructions may be ill-conditioned in the presence of localization errors or high- St particles, which behave ballistically and interact only weakly with the carrier flow, heightening sensitivity to noise. In this section, we systematically examine how seeding density, localization uncertainty, and Stokes number interact to govern the feasibility and robustness of joint reconstructions with inertial tracks.

7.1 Seeding density effects

To start, we examine the influence of particle seeding density. A suite of test cases is generated within a reduced 64^3 HIT domain, varying the seeding density (equivalently, the inter-particle spacing) as described in § 3.4. Both the flow-only and joint estimation methods are tested for comparison. [Figure 18](#) reports the NRMSEs of the reconstructed velocity and pressure fields as functions of normalized inter-particle spacing, σ/l_η . Because the flow-only method neglects particle–fluid coupling, reducing the particle spacing does not improve the conditioning of the problem, and reconstruction accuracy remains poor, with velocity and pressure NRMSEs hovering near 40% and 100%, respectively. The velocity field is not entirely missed, however, since inertial particles ($St = 3$) retain some correlation with large-scale structures through their delayed response. By contrast, joint estimation yields marked improvements as the particle spacing decreases, with e_v and e_p dropping from roughly 20% and 50% to 5% and 10%, respectively. This sharp reduction in error signals a transition from an ill-posed to a well-posed regime. Put differently, given an appropriate inertial transport model and sufficiently dense track data, a DA solver can provide practical means to invert the mapping from flow states to inertial Lagrangian data.

The left side of [figure 19](#) shows normalized spectral errors via (4.5) of the flow-only and joint particle–flow reconstructions, providing a scale-dependent assessment of flow accuracy. Again, Nyquist wavenumbers are plotted to aid interpretation. As seen, errors of the flow-only reconstruction stagnate at a high error level (over 10% across wavenumbers), whereas the joint estimation method achieves exponentially decreasing errors with smaller particle spacings. To better visualize the error trends, we plot the error spectra relative to the respective Nyquist wavenumbers in the right panel of [figure 19](#), which is divided into the sub- and super-Nyquist regions. In the sub-Nyquist region, joint reconstruction outperforms the flow-only approach by increasing margins (up to three orders of magnitude) at lower wavenumbers. This reveals the fundamental limitation of flow-only inversion: not even bulk (low-wavenumber) structures are better reconstructed by adding more particles (or at least not by much). In the super-Nyquist region, while flow-only reconstructions plateau at high errors (NRMSEs exceeding 30%), joint estimation achieves super-resolution at high seeding densities, with errors dropping to 5% beyond the Nyquist wavenumber in the densest case.

As before, particle sizes are jointly inferred through the inertial model. [Figure 20](#) shows normalized PDFs of the initial and optimized d_p values against the ground truth for four representative particle spacings (labels are placed atop each subfigure). At low spacings, optimized d_p values align closely with the true distribution,

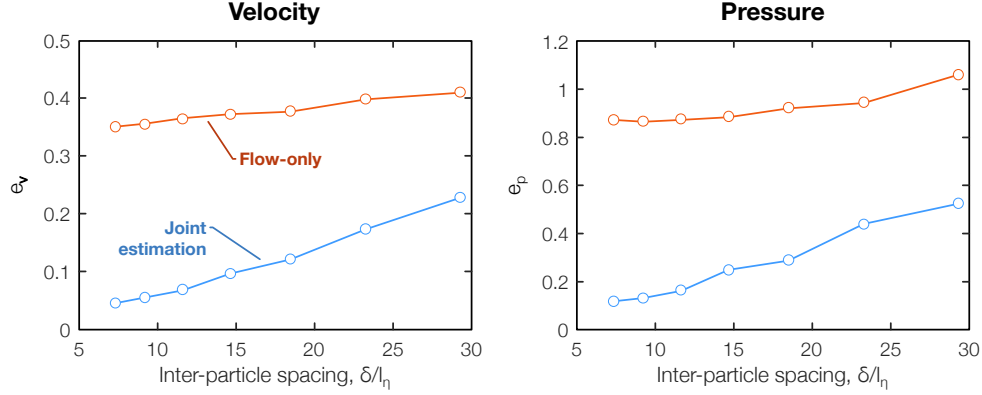


Figure 18: NRMSEs of reconstructed HIT flow fields versus seeding density: (left) velocity; (right) pressure. Flow-only (red) versus joint estimation (blue). Joint estimation errors decrease with higher seeding, marking the transition from an ill-posed problem to a well-posed one.

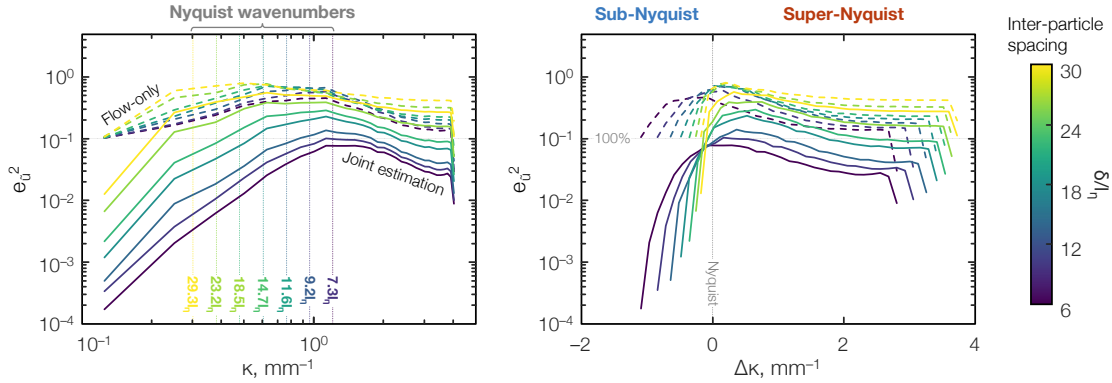


Figure 19: Error spectra of HIT reconstructions under varying inter-particle spacings. Spectra are shown versus wavenumber (left) and normalized by the Nyquist wavenumber (right). Colors denote particle spacing. Dashed lines indicate flow-only reconstructions ($St \rightarrow 0$), solid lines show joint estimation. Errors in joint estimation decay exponentially with increasing seeding density, whereas flow-only reconstructions retain large error across all scales.

while at large spacings the optimization fails to converge, reflecting the poor flow states recovered under sparse seeding. The Pearson correlation coefficient drops from 0.94 to 0.24 between the smallest and largest spacings. As in figures 14 and 17, d_p is systematically underestimated, consistent with the filtering of slip velocities in the reconstructed flow fields. Figure 21 depicts bias and random errors in d_p before and after optimization, where bias is the mean error across particles and random error is the standard deviation. Initial d_p values are unbiased, as expected from the random initialization, whereas optimized values show increasing negative bias with larger spacings, again tied to degraded velocity field reconstructions (see figure 19). Random error, however, is sharply reduced under dense seeding, falling from around $5 \mu\text{m}$ at the sparsest condition to $1.5 \mu\text{m}$ at the highest seeding density.

Together, these results underscore once again the dependence of flow and particle observability upon seeding density. Denser track data enriches the measurement manifold, providing sufficient information to reconstruct the attractor of the flow, under which both flow states and particle properties become recoverable from Lagrangian data via the coupled governing equations of both phases.

7.2 Noise and Stokes number effects

Lastly, we examine how measurement uncertainty and particle inertia interact to shape the joint observability of flow states and particle properties. Inertial tracks with different combinations of noise level and Stokes number (N, St) are reconstructed. The resulting NRMSEs for velocity and pressure are shown in the 3D bar plots of figure 22. Both quantities follow the same trend: they are relatively insensitive to noise at low St but

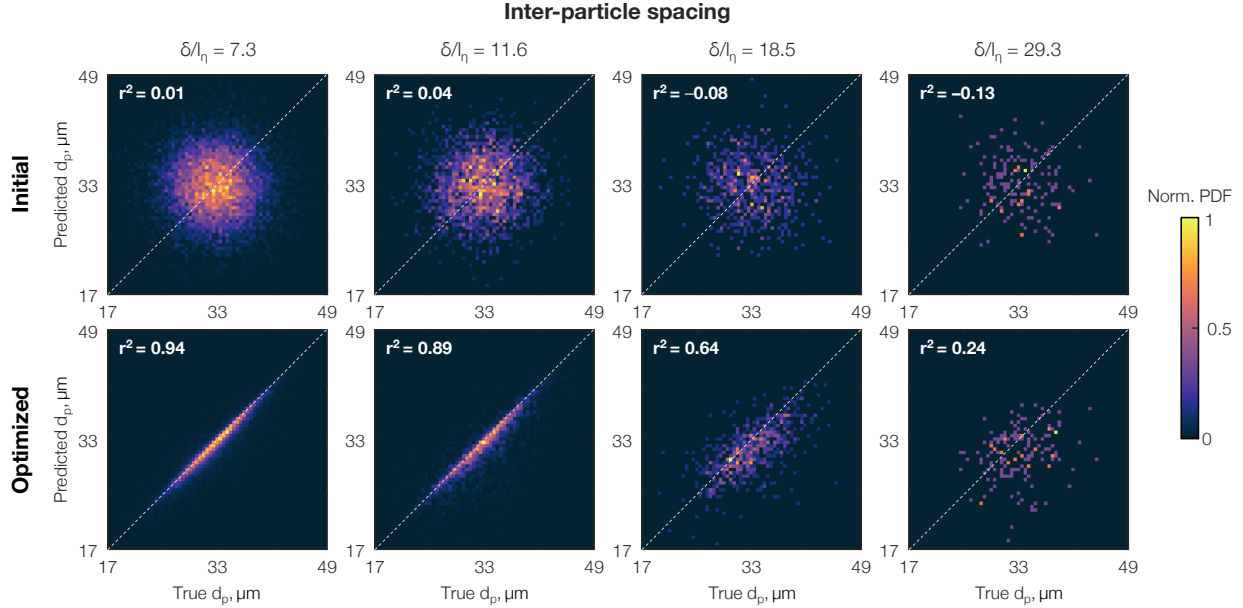


Figure 20: Implicit particle characterization in a reduced HIT domain under varying seeding densities. Initial (top) and optimized (bottom) estimates of d_p compared with the ground truth. At sparse seeding, optimized d_p values diverges from the truth, consistent with poor flow observability.

deteriorate quickly at high St , where errors grow dramatically with added noise. This behavior is expected. To see why, we rearrange the Maxey–Riley equation (B.4) to isolate the carrier velocity,

$$\mathbf{u} = \left(\frac{d\mathbf{v}}{dt} - \mathbf{g} \right) \tau_p + \mathbf{v}. \quad (7.1)$$

In this expression, terms II–IV of (B.4) are neglected owing to the large density ratio, $\rho_p/\rho \sim O(10^3)$. At low St ($\tau_p \rightarrow 0$), this equation reduces to $\mathbf{u} = \mathbf{v}$: the particle velocity directly tracks the fluid velocity, so flow recovery is robust even with noise, as shown earlier in § 5. At high St ($\tau_p \sim O(\tau_\eta)$), however, the acceleration term, $(d\mathbf{v}/dt - \mathbf{g}) \tau_p$, becomes dominant, making \mathbf{u} highly sensitive to errors in particle acceleration. Because acceleration estimates degrade quickly with noise (Berk, 2024), reconstruction accuracy collapses. In the ballistic limit ($\tau_p \rightarrow \infty$), even small errors in acceleration are amplified without bound, rendering the flow effectively *unobservable*: large-inertia particles carry too little imprint of the surrounding flow field to allow for accurate inference thereof.

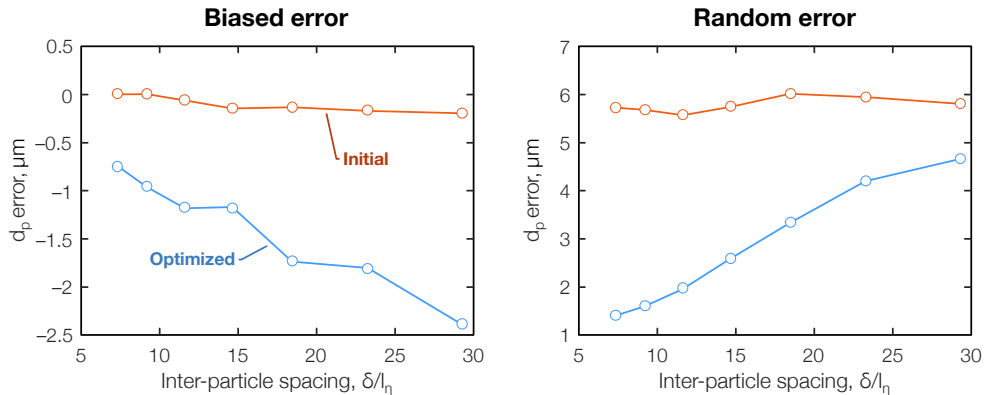


Figure 21: Bias (left) and random (right) errors in d_p before (red) and after (blue) optimization across seeding densities. Both are sharply reduced at high density due to improved flow recovery.

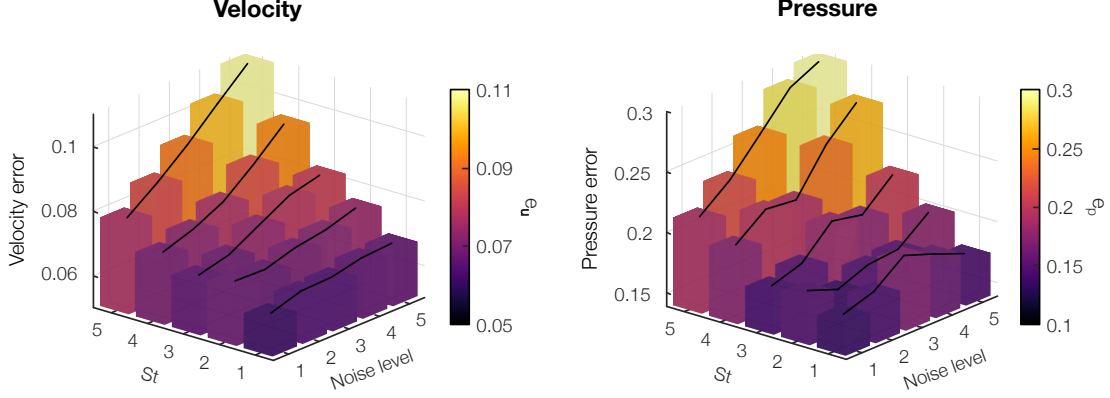


Figure 22: NRMSEs of reconstructed HIT flow fields: (left) velocity; (right) pressure under varying noise levels and Stokes numbers. Accuracy deteriorates with increasing noise and St . In the $St \rightarrow \infty$ limit, flow becomes nearly unobservable due to extreme sensitivity to errors in particle acceleration.

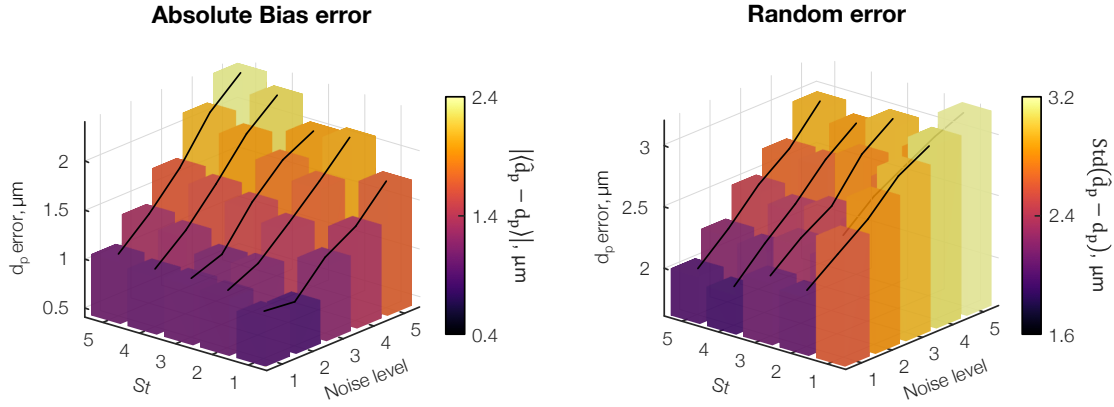


Figure 23: Absolute bias (left) and random (right) errors of inferred particle diameters under varying noise levels and Stokes numbers. Bias increases with noise and St due to filtered velocity fields. Random errors decrease with larger St owing to stronger sensitivity of the physics loss to d_p . In the tracer limit ($St \rightarrow 0$), d_p is nearly unobservable.

Figure 23 shows the absolute bias and random errors of d_p estimates from joint reconstructions. Bias errors increase with both noise level and Stokes number, mirroring the velocity and pressure trends in figure 22. This likely reflects stronger filtering in the reconstructed flow at higher noise and St , which propagates into the particle size estimates. The random errors, however, reveal a more nuanced trend. As expected, they grow with noise, but they decrease at larger St , indicating improved observability of d_p for high-inertia particles, even though flow reconstruction itself worsens, per figure 22. This behavior stems from the particle physics loss (2.7), which becomes more sensitive to d_p at high Stokes numbers. During training, d_p is optimized alongside the flow model to yield values of τ_p (via (B.1)–(B.3)) that minimize the residuals of (7.1). Per (B.2), τ_p scales as $\tau_p \sim \rho_p d_p^{1.313}$ under the Schiller–Naumann drag law, so the sensitivity of τ_p to d_p increases with particle density. Heavy particles are thus more effectively optimized in gradient descent, reducing random errors at high St . The limiting cases illustrate this: when $\tau_p \rightarrow 0$ (ideal tracers), perturbations in d_p barely affect inertia and the true particle size becomes *nearly* unobservable, especially under high positional errors. Nevertheless, the uncertainty about d_p in the $St \rightarrow 0$ limit does not compromise flow reconstruction, since tracer particles track the carrier phase with high fidelity.

Several guidelines for LPT with inertial particles follow from the above sensitivity analyses. First, seeding density should be increased whenever possible to make the problem more well-posed, provided that particle–flow interactions remain in the one-way coupling regime (i.e., to simplify the governing equations) and that tracking is not degraded by image overlap at high densities. Second, low-inertia particles

are generally preferable for accurate flow reconstruction. When only high-inertia particles are available, high-resolution LPT systems are needed to reduce noise and improve acceleration estimates during joint reconstruction. Third, for joint observation of particle properties, reducing measurement noise lowers both bias and random errors in d_p . High seeding density is again advantageous, as it alleviates the implicit filtering effect of the flow and thereby reduces bias in the inferred particle sizes.

8 Concluding remarks

This work investigates the joint observability of flow states and particle properties using Lagrangian track data. The problem is motivated by two central challenges in LPT experiments: noisy particle tracks and inertial transport effects. Existing DA algorithms rely on error-prone velocity estimates derived from fitted tracks and assume ideal tracer particles with zero slip, both of which compromise the fidelity of Eulerian reconstructions. To overcome these limitations, we propose to reconstruct the flow and particle states jointly from track data, under the combined constraints of disperse multiphase flow physics and known localization uncertainties. The resulting framework, termed NIPA, is built on a PINN architecture that couples a neural flow model with a set of kinematics-constrained track models, with one for each particle. Joint training of these models yields flow fields and particle properties—*positions, diameters, densities*—that at once satisfy governing physics and match the LPT data.

We test NIPA across a range of particle-laden flows: incompressible turbulence with ideal tracers in § 5, incompressible turbulence with inertial particles in § 6.1, and compressible, shock-dominated flow with inertial particles in § 6.2. For each case, we ask whether the available track data, together with the governing physics, suffices to recover both flow states and unknown particle properties. In this sense, our results, which demonstrate successful joint reconstructions, constitute empirical existence proofs of joint observability under realistic conditions. We also examine how seeding density, noise magnitude, and Stokes number influence reconstruction robustness in § 7. From these studies, four main conclusions emerge, as summarized below.

1. For noisy tracks of ideal tracers, both flow states and true particle positions are jointly observable in the TBL case, provided a sufficient number of tracks are available (§ 5). Across a broad range of seeding densities, jointly estimated tracks and flow states achieve higher fidelity than filtered tracks or baseline flow-only reconstructions, underscoring the value of coupled flow–particle learning. As seeding density decreases, accuracy inevitably degrades, and conventional filtering may become preferable once Eulerian fields cannot be reliably inferred from tracks of any fidelity. At large localization uncertainties, however, joint flow–particle estimation was found to be robust, outperforming conventional filters by roughly 50%, owing to the integration of physics-based tracking with flow reconstruction.
2. Inertial particle properties are jointly observable with incompressible (§ 6.1) and compressible (§ 6.2) flow states. Reconstructions that account for particle–fluid interactions (e.g., via the Maxey–Riley equation) resolve flow states to high accuracy from inertial tracks, whereas tracer-based assumptions fail. At the same time, particle properties such as diameter are inferred implicitly from tracks and governing physics. Particle density estimation in the compressible case diverges, reflecting weak sensitivity of flow reconstruction to ρ_p , yet without degrading flow accuracy. When particle properties are known and provided for training, flow observability improves substantially, highlighting the complementary relationship between flow and particle inference.
3. The information content of the track data strongly influences joint observability in inertial-particle cases (§ 7.1). Dense seeding enables scale-resolving flow reconstruction, even beyond the particle Nyquist wavenumber, whereas sparse seeding renders the inversion too ill-posed, resulting in heavily filtered flow fields that miss out on most of the high-wavenumber features. These filtered fields further obscure particle observability, leading to systematic underestimation of particle diameters and increasing random errors.
4. Flow and particle observability exhibit a coupled dependence on localization uncertainty and Stokes number (§ 7.2). Reconstruction accuracy declines with increasing noise and St , as expected. At high St , ballistic particles magnify even small acceleration errors through the Maxey–Riley dynamics, rendering the flow *almost* unobservable. Bias errors in inferred particle size also increase with noise and St due to stronger filtering of flow fields. Yet random errors decrease with larger St , since high-inertia particles yield greater sensitivity of the physics loss to changes in d_p . In the tracer limit, particle size is effectively

unobservable, though this lack of information does not compromise flow recovery.

While the framework developed here was designed primarily to demonstrate the existence of joint observability, the concept itself extends beyond *NIPA*. Other DA methods, including adjoint–variational approaches (Zaki, 2025; Zaki & Wang, 2025), could incorporate joint flow–particle observability in principle. More advanced solvers may further enhance performance, particularly in the inertial regime, and thus broaden the range of conditions under which LPT measurements remain informative. Our findings suggest several productive avenues for future work.

1. Apply *NIPA* to real experimental LPT data with inertial particles, to assess robustness under true experimental uncertainties.
2. Extend the framework to learn drag models directly from track data by treating drag coefficients as trainable parameters. This would enable in situ calibration of drag laws, rather than relying on correlations fitted in separate flow conditions.
3. Leverage particle inertia to mitigate non-uniform seeding. In tracer-based experiments, clustering and voids, e.g., near vortex cores (Wolf et al., 2019), can obscure the underlying flow fields. By incorporating inertial particles with distinct spatial distributions, our framework offers a pathway to reconstruct flows under such conditions.

Appendix A Carrier-phase governing equations

Lagrangian particle tracking experiments involve disperse multiphase flows, wherein tracer particles constitute the disperse phase and the fluid of interest is the carrier phase. Depending on the particle mass loading and volume fraction, particle–fluid interactions are modeled using one-way, two-way, or four-way coupling schemes (Subramaniam & Balachandar, 2022). Analysis in this work applies to the one-way coupled regime, where momentum transfer from particles to the carrier flow is negligible. This assumption is appropriate for most PIV and LPT experiments, which typically operate in the dilute limit. Governing equations for flows in the test cases introduced in § 3 are summarized below.

A.1 Equations for unsteady 3D incompressible flow

Flows in the TBL (§ 3.1) and HIT (§ 3.2) cases are governed by the 3D continuity and momentum equations for incompressible flow,

$$\nabla \cdot \mathbf{u} = 0, \quad (\text{A.1a})$$

$$\frac{\partial \mathbf{u}}{\partial t} + \mathbf{u} \cdot \nabla \mathbf{u} = -\frac{1}{\rho} \nabla p + \nu \nabla^2 \mathbf{u} + \mathbf{F}, \quad (\text{A.1b})$$

where \mathbf{u} is the 3D velocity vector and ∇ denotes the del operator in Cartesian coordinates. For isotropic turbulence, a forcing term is introduced to sustain stationary turbulence (Rosales & Meneveau, 2005),

$$\mathbf{F} = \frac{\varepsilon}{3 u_{\text{rms}}^2} \mathbf{u}, \quad (\text{A.2})$$

with ε being the mean energy dissipation rate and u_{rms} the root-mean-square velocity. For the TBL case, we set $\mathbf{F} = \mathbf{0}$. In both the TBL and HIT cases, the residual vector \mathbf{e}_f in (2.6) is formed from the components of (A.1).

A.2 Equations for steady axisymmetric compressible flow

The cone–cylinder flow (§ 3.3) is governed by the steady, axisymmetric compressible Navier–Stokes equations for the conservation of mass, momentum, and energy,

$$\nabla \cdot (\rho \mathbf{u}) = 0, \quad (\text{A.3a})$$

$$\nabla \cdot (\rho \mathbf{u} \mathbf{u}^\top) = -\nabla p + \nabla \cdot \left[\mu (\nabla \mathbf{u} + \nabla \mathbf{u}^\top) - \frac{2}{3} \mu (\nabla \cdot \mathbf{u}) \mathbf{I} \right], \quad (\text{A.3b})$$

$$\nabla \cdot [(\rho E + p) \mathbf{u}] = \nabla \cdot (k \nabla T) + \nabla \cdot \left\{ \left[\mu (\nabla \mathbf{u} + \nabla \mathbf{u}^\top) - \frac{2}{3} \mu (\nabla \cdot \mathbf{u}) \mathbf{I} \right] \cdot \mathbf{u} \right\}. \quad (\text{A.3c})$$

In these expressions, \mathbf{u} denotes the velocity vector with axial and radial components and ∇ is the 2D del operator in cylindrical coordinates (axial–radial). The thermodynamic variables are the density ρ , pressure p ,

and temperature T , while E is the specific total energy and k the thermal conductivity of the carrier phase. The temperature T is obtained from the local total energy and velocity magnitude, and transport properties μ and k are evaluated via Sutherland's law (Anderson, 1990).

Equation (A.3) comprises four governing equations with five unknowns and must therefore be closed with an equation of state. We adopt the calorically perfect gas law,

$$p = (\gamma - 1) \rho \underbrace{\left(E - \frac{1}{2} \mathbf{u} \cdot \mathbf{u} \right)}_{C_v T}, \quad (\text{A.4})$$

where $\gamma = C_p/C_v$ is the ratio of specific heat at constant pressure C_p to that at constant volume C_v . For the cone-cylinder test case, the residual vector e_f in (2.6) collects the contributions from each of the conservation laws in (A.3).

Appendix B Disperse-phase governing equations

This appendix summarizes the particle dynamics models employed for the bidispersed HIT case (§ 3.2) and the supersonic cone-cylinder flow case (§ 3.3). We begin with the full Maxey–Riley equation, which governs the motion of small spherical particles in incompressible fluids. We then outline its modification for compressible flows, relevant to tracer particle dynamics in high-speed PIV/LPT applications. Next, we introduce key dimensionless numbers that quantify the relative importance of viscous, compressibility, and rarefaction effects on particle motion. Finally, we summarize a drag law suitable for supersonic conditions, which incorporates corrections for these effects.

B.1 Maxey–Riley equation

Small spherical particles moving in a locally uniform flow are subject to both inertial and viscous forces. The inertial transport regime is commonly characterized by the particle Reynolds number, defined in terms of a characteristic particle length (diameter d_p), slip velocity, and fluid density and viscosity,

$$Re_p = \frac{\rho d_p \overbrace{|\mathbf{u} - \mathbf{v}|}^{\text{slip}}}{\mu}. \quad (\text{B.1})$$

Here, “slip” refers to the ballistic motion of the particle relative to the carrier fluid. A related measure is the particle response time, which quantifies the time scale at which a particle relaxes toward the local fluid velocity,

$$\tau_p = \frac{4}{3C_D Re_p} \frac{\rho_p d_p^2}{\mu} = \frac{4}{3C_D} \frac{\rho_p}{\rho} \frac{d_p}{|\mathbf{u} - \mathbf{v}|}, \quad (\text{B.2})$$

where C_D is the drag coefficient. In the creeping-flow limit, where $Re_p \ll 1$, Stokes' law applies, with $C_D = 24/Re_p$. For finite Re_p , however, inertial effects necessitate modification of the drag law. For our HIT case, we adopt the Schiller–Naumann correlation,

$$C_D = \frac{24}{Re_p} \left(1 + 0.15 Re_p^{0.687} \right), \quad Re_p < 800, \quad (\text{B.3})$$

which has been validated over a broad range of Re_p . More general drag laws applicable at higher Re_p are reviewed in Chapter 8 of Subramaniam and Balachandar (Subramaniam & Balachandar, 2022) and can be incorporated into the DA framework where applicable.

When particles are much smaller than the relevant hydrodynamic length scale (i.e., quasi-point particles), their dynamics are governed by the version of the Maxey–Riley equation (Maxey et al., 1997) modified by Mei (1996),

$$\frac{d\mathbf{v}}{dt} = \underbrace{\frac{\mathbf{u} - \mathbf{v}}{\tau_p}}_I + \underbrace{\frac{\rho}{\rho_p} \frac{D\mathbf{u}}{Dt}}_{II} + \underbrace{\frac{1}{2} \frac{\rho}{\rho_p} \left(\frac{D\mathbf{u}}{Dt} - \frac{d\mathbf{v}}{dt} \right)}_{III} + \underbrace{\sqrt{\frac{9}{2\pi}} \frac{\rho}{\rho_p \tau_p} \int_{-\infty}^t \frac{1}{\sqrt{t - \tau}} \frac{d(\mathbf{u} - \mathbf{v})}{d\tau} d\tau}_{IV} + \underbrace{\mathbf{g}}_V, \quad (\text{B.4})$$

where D/Dt and d/dt denote total derivatives following a fluid parcel and a particle, respectively. The five terms on the right-hand side correspond to: (I) quasi-steady drag, (II) pressure gradient force, (III) added mass effect, (IV) Basset history term (unsteady vorticity diffusion), and (V) gravitational force. Since the carrier-phase momentum equation, i.e., (A.1b), neglects gravity, buoyancy is not included in (B.4). If gravity were retained, the last term would instead appear as $(1 - \rho/\rho_p)g$, consistent with the formulation of Mei (1996). The relative magnitude of each contribution depends on flow conditions and particle properties (e.g., density, diameter) (Thomas, 1992; Ling et al., 2013).

Two simplifications are made based on the properties of the small, dense particles assumed in our simulations. First, owing to the large particle-to-fluid density ratio, $\rho_p/\rho \sim O(10^3)$, we neglect the Basset history force in the forward simulations (Eaton, 2009; Ling et al., 2013). In the reconstructions, we additionally omit the pressure gradient and added mass forces, which are indeed included in the forward simulations, since their magnitudes are roughly three orders of magnitude smaller than Stokes drag. This deliberate mismatch between the forward and reconstruction force models highlights the robustness of NIPA to imperfect particle dynamics, which is important in practice. Second, given the minute particle size, we neglect finite-size corrections such as the Faxén term and Saffman lift (Maxey et al., 1997). The Kolmogorov length scale in § 3.2 is about $350 \mu\text{m}$: substantially larger than the maximum particle diameter of $\sim 70 \mu\text{m}$, thereby justifying the quasi-point-particle assumption. Consequently, for the HIT case, the residual vector $e_p^{(k)}$ in (2.7) includes only the contributions from Stokes drag and gravity, i.e., terms (I) and (V) in (B.4), for the k th particle.

B.2 Particle dynamics in compressible flows

Tracer particles in high-speed flow are often modeled as solid spheres immersed in an unbounded fluid and subject only to quasi-steady drag (Williams et al., 2015). For typical tracers in PIV or LPT, i.e., very small ($d_p \sim 1 \mu\text{m}$) and with large density ratios ($\rho_p/\rho \gg 1$), the contributions of pressure gradient, added mass, Basset history, and body forces are negligible in high-speed conditions (Melling, 1997; Ragni et al., 2011). Under these assumptions, the Maxey–Riley equation reduces to a balance between slip velocity and quasi-steady drag,

$$\frac{dv}{dt} = \frac{\mathbf{u} - \mathbf{v}}{\tau_p}, \quad (\text{B.5})$$

where τ_p is the particle response time given in (B.2). In our supersonic cone flow case, \mathbf{u} and \mathbf{v} are 2D vectors (axial and radial), and the residual $e_p^{(k)}$ in (2.7) comprises both components of (B.5) for the k th particle. Although pressure gradient, added mass, and Basset history forces can momentarily exceed Stokes drag as particles traverse a shock wave, their cumulative effect on particle trajectories is negligible in the high-density-ratio limit (Thomas, 1992; Parmar et al., 2009; Capecehatro & Wagner, 2023), making them safe to neglect for our purposes.

B.3 Compressible drag law

Particle drag in high-speed flow depends not only on viscous forces from the carrier phase but also on compressibility and rarefaction effects. Compressibility effects scale with the particle Mach number,

$$Ma_p = \frac{|\mathbf{u} - \mathbf{v}|}{\sqrt{\gamma RT}}, \quad (\text{B.6})$$

where R is the specific gas constant of the carrier phase. Rarefaction effects are governed by the ratio of the mean free path of the carrier fluid, λ , to a characteristic length scale, typically the particle diameter at low Re_p . This ratio defines the particle Knudsen number,

$$Kn_p = \frac{\lambda}{d_p} = \frac{Ma_p}{Re_p} \sqrt{\frac{\pi\gamma}{2}}, \quad (\text{B.7})$$

where the expression on the right-hand side follows from the ideal gas law. Thus, drag correlations for compressible particle-laden flows can be expressed in terms of any two of the three nondimensional groups: Re_p , Ma_p , and Kn_p . In practice, this formulation allows models such as Loth’s drag law, discussed next, to bridge viscous, compressibility-dominated, and rarefaction-dominated regimes.

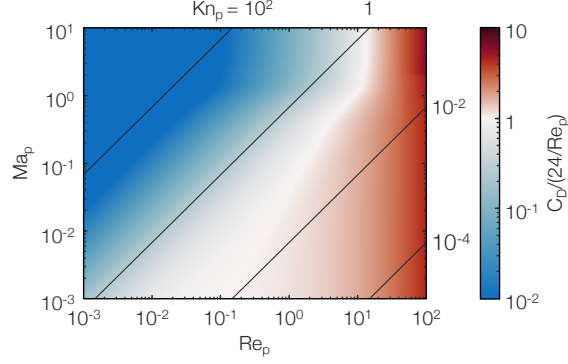


Figure 24: Loth drag model normalized by Stokes drag, showing dependence on Re_p and Ma_p . Black lines indicate isocontours of Kn_p .

Loth (2008) put forth a comprehensive drag correlation for compressible particle-laden flows. The model expresses the drag coefficient C_D as a function of particle Reynolds and Mach numbers, thereby defining the particle response time τ_p through (B.2). The general form is

$$C_D = \begin{cases} \frac{C_{D,Kn,Re}}{1 + Ma_p^4} + \frac{Ma_p^4 C_{D,f_M,Re}}{1 + Ma_p^4}, & Re_p < 45 \\ \frac{24}{Re_p} \left[1 + 0.15 Re_p^{0.687} \right] H_M + \frac{0.42 C_M}{1 + \frac{42 \cdot 500 G_M}{Re_p^{1.16}}}, & Re_p > 45 \end{cases}. \quad (B.8)$$

The first branch of (B.8) applies in the rarefaction-dominated regime ($Re_p < 45$) and the second branch in the compression-dominated regime ($Re_p > 45$). Although we implement the full model in forward simulations, the cone-cylinder case has $Re_p < 23$ throughout, so only the rarefaction branch is used in our reconstructions. Figure 24 shows C_D normalized by Stokes drag as a function of Re_p and Ma_p . At low Re_p , contours of C_D align with those of Kn_p , indicating rarefaction control. As Re_p increases, the gradient of $C_D Re_p / 24$ bends toward the Ma_p axis, marking the onset of compressibility effects. In our case, however, the flow remains entirely within the aforementioned rarefaction regime.

Returning to (B.8), the rarefaction-specific terms are

$$C_{D,Kn,Re} = \frac{24}{Re_p} \left(1 + 0.15 Re_p^{0.687} \right) f_{Kn}, \quad (B.9a)$$

$$f_{Kn} = \frac{1}{1 + Kn_p \left[2.514 + 0.8 \exp\left(-\frac{0.55}{Kn_p}\right) \right]}, \quad (B.9b)$$

$$C_{D,f_M,Re} = \frac{C_{D,f_M}}{1 + \left(\frac{C_{D,f_M}}{1.63} - 1 \right) \sqrt{\frac{Re_p}{45}}}, \quad (B.9c)$$

$$C_{D,f_M} = \frac{(1 + 2s_M^2) \operatorname{erf}(-s_M^2)}{s_M^3 \sqrt{\pi}} + \frac{(4s_M^4 + 4s_M^2 - 1) \operatorname{erf}(s)}{2s_M^4} + \frac{2}{3s_M} \sqrt{\frac{\pi T_p}{T}}, \quad (B.9d)$$

$$s_M \equiv Ma_p \sqrt{\gamma/2}, \quad (B.9e)$$

where T_p is the particle temperature. The compression-specific contributions to (B.8) are

$$H_M = 1 - \frac{0.258 C_M}{1 + 514 G_M}, \quad (\text{B.10a})$$

$$G_M = \begin{cases} 1 - 1.525 Ma_p^4, & Ma_p < 0.89 \\ 0.0002 + 0.0008 \tanh[12.77 (Ma_p - 2.02)], & Ma_p > 0.89 \end{cases}, \quad (\text{B.10b})$$

$$C_M = \begin{cases} \frac{5}{3} + \frac{2}{3} \tanh[3 \log(Ma_p - 0.1)], & Ma_p < 1.45 \\ 2.044 + 0.2 \exp\left[-1.8 \log\left(\frac{Ma_p}{1.5}\right)^2\right], & Ma_p > 1.45 \end{cases}. \quad (\text{B.10c})$$

The resultant drag law has been extensively benchmarked using experimental data and employed for many simulations of high-speed particle-laden flow. Recently, Loth et al. (2021) published a comprehensive review of relevant results, obtained from particle-resolved DNSs, rarefied-gas simulations, and wind tunnel experiments. The authors found that Loth's original model was not empirically supported near $Re_p = 45$. They reported an updated model that corrects for these discrepancies in Loth et al. (2021). However, updates in that paper do not meaningfully affect the cone-cylinder simulation in § 3.3 because, again, it has a maximum Re_p of about 23. We thus employ the original formulation of Loth (2008), as presented above.

Appendix C B-spline filtering

For the baseline flow-only reconstruction defined in § 2.2.4, particle velocities are estimated from measured tracks via finite differencing as well as smoothing. Among available options, cubic B-splines provide a standard filtering approach because they yield C^2 -continuous fits with good stability while relying only on low-order piecewise polynomials (Gesemann et al., 2016; Li et al., 2024). A representative cubic B-spline approximation for the x -coordinate of a particle trajectory is

$$\hat{x}(t) = \sum_{j=0}^K c_j \alpha\left(\frac{t - t'_j}{\Delta t}\right), \quad (\text{C.1})$$

where c_j are spline coefficients, $\{t'_j \mid j = 0, \dots, K\}$ are uniformly spaced knots with spacing Δt , and α denotes the cubic basis function (Skare & Andersson, 2005),

$$\alpha(t) = \begin{cases} \frac{2}{3} - \left(1 - \frac{|t|}{2}\right) t^2, & 0 < |t| < 1 \\ \frac{(2 - |t|)^3}{6}, & 1 < |t| < 2 \\ 0, & |t| > 2 \end{cases}. \quad (\text{C.2})$$

Velocity and acceleration are then obtained analytically as the first and second derivatives of \hat{x} . Naturally, the same construction applies to the other spatial components.

The number of knots K controls the trade-off between smoothness and fidelity. Increasing K improves the ability of the spline to follow fine-scale fluctuations but risks fitting to measurement noise. Conversely, small- K splines over-smooth the trajectories. In practice, we set K adaptively such that each spline segment spans about ten measured points, a choice tuned to ensure sufficient expressivity while effectively suppress measurement noise. The spline coefficients are obtained by minimizing the residual between measured and filtered positions in a least-squares sense, i.e., by minimizing

$$\sum_{j=1}^{n_k} \left\| x_j^{(k)} - \hat{x}(t_j) \right\|_2^2,$$

where $x_j^{(k)}$ is the measured position at the j th time step t_j , \hat{x} is the spline estimate from (C.1) evaluated at the same time, and n_k is the total number of points in the track.

In our implementation, filtering is performed via MATLAB's `spap2` and `fnder` routines. While details of software usage are secondary, the essential point here is that B-spline filtering yields smoothed particle tracks from which velocities and accelerations can be determined in a consistent manner. These filtered quantities serve as inputs to the baseline reconstruction method introduced in § 2.2.4, used for comparison throughout our observability tests.

Appendix D Initialization of the KCT models

D.1 Track splitting

Particle tracks in LPT vary in length, ranging from only a few positions to several hundred. Since TensorFlow requires fixed tensor shapes for computational graphs, we divide each trajectory into fixed-length segments of 20 positions. Shorter segments are zero-padded. When a single trajectory spans multiple segments, its particle properties (e.g., size, density) are shared across all segments; these properties may be trainable in cases with inertial particles. Although longer segments are possible, they increase the number and dimension of coefficient matrices in (2.26)–(2.27), thereby raising the computational cost and memory demand of KCTs. Conversely, very short segments disrupt the continuity of tracks and introduce boundary-related artifacts. In practice, therefore, segment lengths of 15–30 points strike a good balance between efficiency and fidelity.

D.2 Warm-starting KCTs with filtered tracks

For inertial particles, joint optimization of flow states, particle positions, and per-particle properties from noisy data is ill-posed and prone to divergence. To improve stability, we “warm-start” each KCT model using filtered tracks obtained from a conventional smoothing technique, such as polynomial regression or kernel convolution (Berk, 2024). Initialization is posed as a per-track optimization that identifies the displacement vector δ and velocity parameters θ which minimize

$$\mathcal{J}_{\text{warm}} = \sum_{j=1}^{n_k} \left(\|v_j - \hat{v}_j\|_2^2 + \chi \|a_j - \hat{a}_j\|_2^2 \right), \quad (\text{D.1})$$

where χ balances velocity and acceleration residuals and is assigned as

$$\chi = \frac{\langle \|\hat{v}\|_2 \rangle_p}{\langle \|\hat{a}\|_2 \rangle_p}, \quad (\text{D.2})$$

with $\langle \cdot \rangle_p$ indicating an average over the current track. Velocities v and accelerations a are the outputs of the particle model $P^{(k)}$ from (2.25) and (2.27).

We minimize (D.1) using MATLAB’s implementation of the Levenberg–Marquardt algorithm, initializing δ with raw (noisy, observed) positions and θ with zeros. In this study, fifth-order polynomials provide the filtered velocity and acceleration vectors \hat{v} and \hat{a} , though more advanced methods such as TrackFit (Gesemann et al., 2016) could also be employed. This warm-start is only used for cases with inertial particles. For ideal tracers, initializing with filtered tracks offers no improvement and risks biasing the reconstruction, so we simply initialize δ with raw data and θ with zeros.

D.3 Particle property transform

In inertial cases, particle properties such as their size and density can differ in units and span several orders of magnitude, limiting the precision of optimization. Therefore, we map each positive property $\varphi > 0$ to a dimensionless variable $\zeta \sim O(1)$, with the latter variable being optimized. The forward transformation is

$$\zeta = \frac{\log[\exp(c_1\varphi) - 1]}{c_2} - c_3, \quad (\text{D.3})$$

with parameters c_1 , c_2 , and c_3 chosen so that ζ is order one. The inverse transform recovers φ ,

$$\varphi = \frac{\log[\exp(c_2\zeta + c_2c_3) + 1]}{c_1} = \frac{\text{softplus}(c_2\zeta + c_2c_3)}{c_1}, \quad (\text{D.4})$$

where the softplus function ensures that $\varphi > 0$ for $c_1 > 0$.

Parameters are chosen as follows. First, c_1 is set to φ^{-1} , so $c_1\varphi = 1$. Second, given an expected range $\varphi \in [\varphi_{\min}, \varphi_{\max}]$, we determine c_2 and c_3 by enforcing $\zeta(\varphi_{\min}) = -1$ and $\zeta(\varphi_{\max}) = 1$, yielding

$$c_2 = \frac{\log[\exp(c_1\varphi_{\min}) - 1]}{c_3 - 1}, \quad c_3 = \frac{2}{1 - \zeta} - 1, \quad (\text{D.5a})$$

with

$$\zeta = \frac{\log[\exp(c_1\varphi_{\min}) - 1]}{\log[\exp(c_1\varphi_{\max}) - 1]}. \quad (\text{D.5b})$$

This mapping is bijective and has bounded gradients, ensuring one-to-one correspondence between ψ and ξ and stable optimization during backpropagation. The formulation is valid for strictly positive (or negative) properties such as size and density; properties that may cross zero, such as electrical charge, require a different mapping.

References

- Agüí, J. C. & Jimenez, J. 1987 On the performance of particle tracking. *J. Fluid Mech.* **185**, 447–468.
- Anderson, J. D. 1990 *Modern Compressible Flow: With Historical Perspective*, vol. 12. McGraw-Hill New York.
- Argyropoulos, C. D. & Markatos, N. 2015 Recent advances on the numerical modelling of turbulent flows. *Appl. Math. Model.* **39** (2), 693–732.
- Bec, J. 2003 Fractal clustering of inertial particles in random flows. *Phys. fluids* **15** (11), L81–L84.
- Beresh, S. J. 2021 Time-resolved particle image velocimetry. *Meas. Sci. Technol.* **32** (10), 102003.
- Beresh, S. J., Spillers, R., Soehnel, M. & Spitzer, S. 2020 Extending the frequency limits of postage-stamp PIV to MHz rates. In *AIAA SciTech 2020 Forum*, p. 1018.
- Berk, T. 2024 A second-order polynomial kernel outperforms Gaussian kernels when smoothing Lagrangian particle trajectories. *Exp. Fluids* **65** (7), 1–4.
- Bewley, G. P., Saw, E.-W. & Bodenschatz, E. 2013 Observation of the sling effect. *New J. Phys.* **15** (8), 083051.
- Boiko, V. M., Zapryagaev, V. I., Pivovarov, A. A. & Poplavski, S. V. 2015 Correction of PIV data for reconstruction of the gas velocity in a supersonic underexpanded jet. *Combust. Explos. Shock Waves* **51**, 587–596.
- Brandt, L. & Coletti, F. 2022 Particle-laden turbulence: progress and perspectives. *Annu. Rev. Fluid Mech.* **54**, 159–189.
- Bristow, N., Li, J., Hartford, P., Guala, M. & Hong, J. 2023 Imaging-based 3D particle tracking system for field characterization of particle dynamics in atmospheric flows. *Exp. Fluids* **64** (4), 78.
- Buchta, D. A., Laurence, S. J. & Zaki, T. A. 2022 Assimilation of wall-pressure measurements in high-speed flow over a cone. *J. Fluid Mech.* **947**, R2.
- Capecelatro, J. & Wagner, J. L. 2023 Gas–Particle Dynamics in High-Speed Flows. *Annu. Rev. Fluid Mech.* **56**.
- Cary, A. W., Chawner, J., Duque, E. P., Gropp, W., Kleb, W. L., Kolonay, R. M., Nielsen, E. & Smith, B. 2021 CFD vision 2030 road map: Progress and perspectives. In *AIAA AVIATION 2021 Forum*, p. 2726.
- Casa, L. D. C. & Krueger, P. S. 2013 Radial basis function interpolation of unstructured, three-dimensional, volumetric particle tracking velocimetry data. *Meas. Sci. Technol.* **24** (6), 065304.
- Corrsin, S. 1951 On the spectrum of isotropic temperature fluctuations in an isotropic turbulence. *J. Appl. Phys.* **22** (4), 469–473.
- Deng, Z., He, C., Wen, X. & Liu, Y. 2018 Recovering turbulent flow field from local quantity measurement: turbulence modeling using ensemble-Kalman-filter-based data assimilation. *J. Vis.* **21** (6), 1043–1063.
- Di Leoni, P. C., Agarwal, K., Zaki, T. A., Meneveau, C. & Katz, J. 2023 Reconstructing turbulent velocity and pressure fields from under-resolved noisy particle tracks using physics-informed neural networks. *Exp. Fluids* **64** (5), 95.
- Domínguez-Vázquez, D., Escobar-Castaneda, N., Wang, Q. & Jacobs, G. B. 2025 Inference of inertial particle dynamics from limited measurements. *Phys. Fluids* **37** (4).
- Du, Y., Wang, M. & Zaki, T. A. 2023 State estimation in minimal turbulent channel flow: a comparative study of 4DVar and PINN. *Int. J. Heat Fluid Flow.* **99**, 109073.

- Duraisamy, K., Iaccarino, G. & Xiao, H. 2019 Turbulence modeling in the age of data. *Annu. Rev. Fluid Mech.* **51** (1), 357–377.
- Eaton, J. K. 2009 Two-way coupled turbulence simulations of gas-particle flows using point-particle tracking. *Int. J. Multiph. Flow* **35** (9), 792–800.
- Elghobashi, S. 1994 On predicting particle-laden turbulent flows. *Appl. Sci. Res.* **52**, 309–329.
- Fahringer, T. W., Lynch, K. P. & Thurow, B. S. 2015 Volumetric particle image velocimetry with a single plenoptic camera. *Meas. Sci. Technol.* **26** (11), 115201.
- Faiella, M., Macmillan, C. G. J., Whitehead, J. P. & Pan, Z. 2021 Error propagation dynamics of velocimetry-based pressure field calculations (2): on the error profile. *Meas. Sci. Technol.* **32** (8), 084005.
- Faleiros, D. E., Tuinstra, M., Sciacchitano, A. & Scarano, F. 2021 The slip velocity of nearly neutrally buoyant tracers for large-scale PIV. *Exp. Fluids* **62** (9), 186.
- Fischer, R. D., Moaven, M., Kelly, D., Morris, S., Thurow, B. & Prorok, B. C. 2022 3D tracking velocimetry of L-PBF spatter particles using a single high-speed plenoptic camera. *Addit. Manuf. Lett.* **3**, 100083.
- Foures, D. P. G., Dovetta, N., Sipp, D. & Schmid, P. J. 2014 A data-assimilation method for Reynolds-averaged Navier–Stokes-driven mean flow reconstruction. *J. Fluid Mech.* **759**, 404–431.
- Gao, J., Guildenbecher, D. R., Reu, P. L. & Chen, J. 2013 Uncertainty characterization of particle depth measurement using digital in-line holography and the hybrid method. *Opt. Express* **21** (22), 26432–26449.
- Gesemann, S., Huhn, F., Schanz, D. & Schröder, A. 2016 From noisy particle tracks to velocity, acceleration and pressure fields using B-splines and penalties. In *18th International Symposium on Applications of Laser and Imaging Techniques to Fluid Mechanics*, vol. 4, pp. 1–17.
- Gorlé, C., Garcia-Sanchez, C. & Iaccarino, G. 2015 Quantifying inflow and RANS turbulence model form uncertainties for wind engineering flows. *J. Wind Eng. Ind. Aerodyn.* **144**, 202–212.
- Gronskis, A., Heitz, D. & Mémin, E. 2013 Inflow and initial conditions for direct numerical simulation based on adjoint data assimilation. *J. Comput. Phys.* **242**, 480–497.
- Guo, T., Ardekani, A. M. & Vlachos, P. P. 2019 Microscale, scanning defocusing volumetric particle-tracking velocimetry. *Exp. Fluids* **60**, 1–14.
- Hall, E. M., Guildenbecher, D. R. & Thurow, B. S. 2017 Uncertainty characterization of particle location from refocused plenoptic images. *Opt. Lett.* **25** (18), 21801–21814.
- He, C., Li, S. & Liu, Y. 2025 Data assimilation: new impetus in experimental fluid dynamics. *Exp. Fluids* **66**, 94.
- He, C., Zeng, X., Wang, P., Wen, X. & Liu, Y. 2024 Four-dimensional variational data assimilation of a turbulent jet for super-temporal-resolution reconstruction. *J. Fluid Mech.* **978**, A14.
- Huang, J., Li, S., Zi, Y., Qian, Y., Cai, W., Aldén, M. & Li, Z. 2021 Clustering-based particle detection method for digital holography to detect the three-dimensional location and in-plane size of particles. *Meas. Sci. Technol.* **32** (5), 055205.
- Jeon, Y. J., Schneiders, J. F. G., Müller, M., Michaelis, D. & Wieneke, B. 2018 4D flow field reconstruction from particle tracks by VIC+ with additional constraints and multigrid approximation. In *Proceedings 18th International Symposium on Flow Visualization*, p. 1. ETH Zurich.
- Jerri, A. J. 1977 The Shannon sampling theorem—Its various extensions and applications: A tutorial review. *Proc. IEEE* **65** (11), 1565–1596.
- Johnson, C., Mysore, P. V., Schau, K. A. & Oefelein, J. 2023 Sensitivity of Shock-Wave Boundary-Layer Interactions to Inflow Turbulence Characteristics using the Synthetic Eddy Method. In *AIAA SciTech 2023 Forum*, p. 0094.

- Jux, C., Sciacchitano, A. & Scarano, F. 2020 Flow pressure evaluation on generic surfaces by robotic volumetric PTV. *Meas. Sci. Technol.* **31** (10), 104001.
- Katz, J. & Sheng, J. 2010 Applications of holography in fluid mechanics and particle dynamics. *Annu. Rev. Fluid Mech.* **42**, 531–555.
- Khalitov, D. A. & Longmire, E. K. 2002 Simultaneous two-phase PIV by two-parameter phase discrimination. *Exp. Fluids* **32** (2), 252–268.
- Koike, S., Takahashi, H., Tanaka, K., Hirota, M., Takita, K. & Masuya, G. 2007 Correction method for particle velocimetry data based on the Stokes drag law. *AIAA J.* **45** (11), 2770–2777.
- Kolmogorov, A. N. 1941 The local structure of turbulence in incompressible viscous fluid for very large Reynolds numbers. *Doklady Akademii Nauk SSSR* **30** (4), 299–301.
- Leake, C., Johnson, H. & Mortari, D. 2022 *The Theory of Functional Connections: A Functional Interpolation Framework with Applications*. Lulu.com.
- Li, J., Guala, M. & Hong, J. 2022 Snow particle analyzer for simultaneous measurements of snow density and morphology. *arXiv preprint arXiv:2209.11129*.
- Li, J., Guala, M. & Hong, J. 2024 Field investigation of 3-D snow settling dynamics under weak atmospheric turbulence. *J. Fluid Mech.* **997**, A33.
- Li, L. & Pan, Z. 2024 Three-dimensional time-resolved Lagrangian flow field reconstruction based on constrained least squares and stable radial basis function. *Exp. Fluids* **65** (4), 57.
- Ling, Y., Parmar, M. & Balachandar, S. 2013 A scaling analysis of added-mass and history forces and their coupling in dispersed multiphase flows. *Int. J. Multiph. Flow* **57**, 102–114.
- Loth, E. 2008 Compressibility and rarefaction effects on drag of a spherical particle. *AIAA J.* **46** (9), 2219–2228.
- Loth, E., Daspit, J. T., Jeong, M., Nagata, T. & Nonomura, T. 2021 Supersonic and hypersonic drag coefficients for a sphere. *AIAA J.* **59** (8), 3261–3274.
- Malik, N. A. & Dracos, T. 1995 Interpolation schemes for three-dimensional velocity fields from scattered data using Taylor expansions. *J. Comput. Phys.* **119** (2), 231–243.
- Mallery, K. & Hong, J. 2019 Regularized inverse holographic volume reconstruction for 3D particle tracking. *Opt. Express* **27** (13), 18069–18084.
- Manovski, P., Novara, M., Mohan, N. K. D., Geisler, R., Schanz, D., Agocs, J., Godbersen, P. & Schröder, A. 2021 3D Lagrangian particle tracking of a subsonic jet using multi-pulse Shake-The-Box. *Exp. Therm. Fluid Sci.* **123**, 110346.
- Maxey, M. R., Patel, B. K., Chang, E. J. & Wang, L. P. 1997 Simulations of dispersed turbulent multiphase flow. *Fluid Dyn. Res.* **20** (1-6), 143.
- Maxey, M. R. & Riley, J. J. 1983 Equation of motion for a small rigid sphere in a nonuniform flow. *Phys. Fluids* **26** (4), 883–889.
- Mei, R. 1996 Velocity fidelity of flow tracer particles. *Exp. Fluids* **22** (1), 1–13.
- Melling, A. 1997 Tracer particles and seeding for particle image velocimetry. *Meas. Sci. Technol.* **8** (12), 1406.
- Molnar, J. P., Grauer, S. J., Léon, O., Donjat, D. & Nicolas, F. 2023 Physics-informed background-oriented schlieren of turbulent underexpanded jets. In *AIAA SciTech 2023 Forum*, p. 2441.
- Muralidhar, K. 2002 Temperature field measurement in buoyancy-driven flows using interferometric tomography. *Annu. Rev. Heat Transf.* **12**.

- Nie, M., Whitehead, J. P., Richards, G., Smith, B. L. & Pan, Z. 2022 Error propagation dynamics of PIV-based pressure field calculation (3): What is the minimum resolvable pressure in a reconstructed field? *Exp. Fluids* **63** (11), 168.
- Novara, M., Schanz, D., Geisler, R., Gesemann, S., Voss, C. & Schröder, A. 2019 Multi-exposed recordings for 3D Lagrangian particle tracking with multi-pulse Shake-The-Box. *Exp. Fluids* **60**, 1–19.
- Obukhov, A. M. 1949 The local structure of atmospheric turbulence. *Dokl. Akad. Nauk. SSSR* **67** (4), 643–646.
- Pan, Z., Whitehead, J., Thomson, S. & Truscott, T. 2016 Error propagation dynamics of PIV-based pressure field calculations: how well does the pressure Poisson solver perform inherently? *Meas. Sci. Technol.* **27** (8), 084012.
- Parmar, M., Haselbacher, A. & Balachandar, S. 2009 Modeling of the unsteady force for shock–particle interaction. *Shock Waves* **19**, 317–329.
- Perlman, E., Burns, R., Li, Y. & Meneveau, C. 2007 Data exploration of turbulence simulations using a database cluster. In *Proceedings of the 2007 ACM/IEEE Conference on Supercomputing*, pp. 1–11.
- Raffel, M., Willert, C. E., Scarano, F., Kähler, C. J., Wereley, S. T. & Kompenhans, J. 2018 Physical and technical background. In *Particle Image Velocimetry: A Practical Guide*, pp. 33–111. Springer.
- Ragni, D., Schrijer, F., van Oudheusden, B. W. & Scarano, F. 2011 Particle tracer response across shocks measured by PIV. *Exp. Fluids* **50**, 53–64.
- Raissi, M., Perdikaris, P. & Karniadakis, G. E. 2019 Physics-informed neural networks: A deep learning framework for solving forward and inverse problems involving nonlinear partial differential equations. *J. Comput. Phys.* **378**, 686–707.
- Rival, D. E. & van Oudheusden, B. 2017 Load-estimation techniques for unsteady incompressible flows. *Exp. Fluids* **58** (3), 20.
- Rosales, C. & Meneveau, C. 2005 Linear forcing in numerical simulations of isotropic turbulence: Physical space implementations and convergence properties. *Phys. Fluids* **17** (9), 095106.
- Roy, C. J. & Blottner, F. G. 2006 Review and assessment of turbulence models for hypersonic flows. *Prog. Aerosp. Sci.* **42** (7-8), 469–530.
- Samimy, M. & Lele, S. K. 1991 Motion of particles with inertia in a compressible free shear layer. *Phys. Fluids A: Fluid Dynamics* **3** (8), 1915–1923.
- Scarano, F. 2012 Tomographic PIV: principles and practice. *Meas. Sci. Technol.* **24** (1), 012001.
- Schanz, D., Gesemann, S. & Schröder, A. 2016 Shake-The-Box: Lagrangian particle tracking at high particle image densities. *Exp. Fluids* **57** (5), 1–27.
- Schanz, D., Schröder, A., Gesemann, S., Huhn, F., Novara, M., Geisler, R., Manovski, P. & Depuru-Mohan, K. 2018 Recent advances in volumetric flow measurements: high-density particle tracking ('Shake-The-Box') with Navier–Stokes regularized interpolation ('FlowFit'). *New Results in Numerical and Experimental Fluid Mechanics XI* pp. 587–597.
- Schiller, V. L. 1933 Über die grundlegenden Berechnungen bei der Schwerkraftaufbereitung. *Z. Vereines Deutscher Inge.* **77**, 318–321.
- Schneiders, J. F. G., Scarano, F. & Elsinga, G. E. 2017 Resolving vorticity and dissipation in a turbulent boundary layer by tomographic PTV and VIC+. *Exp. Fluids* **58** (4), 1–14.
- Schröder, A., Geisler, R., Sieverling, A., Wieneke, B., Henning, A., Scarano, F., Elsinga, G. E. & Poelma, C. 2009 Lagrangian aspects of coherent structures in a turbulent boundary layer flow using TR-Tomo PIV and PTV. In *Proceedings of 8th International Symposium on Particle Image Velocimetry*, pp. 25–28.

- Schröder, A. & Schanz, D. 2023 3D Lagrangian particle tracking in fluid mechanics. *Annu. Rev. Fluid Mech.* **55**, 511–540.
- Schröder, A., Schanz, D., Geisler, R., Godbersen, P., Agocs, J. & Simhan, A. R. 2024 Near-wall flow features in ZPG-TBL at various Reynolds numbers using dense 3D Lagrangian Particle Tracking. In *21st International Symposium on the Application of Laser and Imaging Techniques to Fluid Mechanics*, p. 1.
- Schröder, A., Schanz, D., Gesemann, S., Huhn, F., Garaboa-Paz, D. & Bodenschatz, E. 2022 Measurements of the energy dissipation rate in homogeneous turbulence using dense 3D Lagrangian Particle Tracking and FlowFit. In *Proceedings of the 20th International Symposium on the Application of Laser and Imaging Techniques to Fluid Mechanics*, 1 216, pp. 2300–2319.
- Schröder, A., Schanz, D., Michaelis, D., Cierpka, C., Scharnowski, S. & Kähler, C. J. 2015 Advances of PIV and 4D-PTV “Shake-The-Box” for turbulent flow analysis—the flow over periodic hills. *Flow Turbul. Combust.* **95**, 193–209.
- Shin, H. & Schröder, A. 2025 Robust flow field reconstruction using PINN for 3D Lagrangian particle tracking. In *16th International Symposium on Particle Image Velocimetry*, 1 1142, pp. 1–12.
- Skare, S. & Andersson, J. 2005 Correction of MR image distortions induced by metallic objects using a 3D cubic B-spline basis set: application to stereotactic surgical planning. *Magn. Reson. Med.* **54** (1), 169–181.
- Slotnick, J. P., Khodadoust, A., Alonso, J., Darmofal, D., Gropp, W., Lurie, E. & Mavriplis, D. J. 2014 CFD Vision 2030 Study: A Path to Revolutionary Computational Aerosciences. *Tech. Rep.* NF1676L-18332. National Aeronautics and Space Administration.
- Subramaniam, S. & Balachandar, S. 2022 *Modeling Approaches and Computational Methods for Particle-laden Turbulent Flows*. Academic Press.
- Tancik, M., Srinivasan, P., Mildenhall, B., Fridovich-Keil, S., Raghavan, N., Singhal, U., Ramamoorthi, R., Barron, J. & Ng, R. 2020 Fourier features let networks learn high frequency functions in low dimensional domains. *NeurIPS* **33**, 7537–7547.
- Tang, R., Zhou, K., Tan, J. & Grauer, S. J. 2025 Neural inference of fluid-structure interactions from sparse off-body measurements. *arXiv preprint arXiv:2506.23480* .
- Thomas, P. 1992 On the influence of the Basset history force on the motion of a particle through a fluid. *Phys. Fluids* **4** (9), 2090–2093.
- Toloui, M. & Hong, J. 2015 High fidelity digital inline holographic method for 3D flow measurements. *Opt. Express* **23** (21), 27159–27173.
- de la Torre, R. G. R. & Jensen, A. 2023 Sizing of particles and droplets using 3D-PTV, an OpenPTV post-processing tool. *Meas. Sci. Technol.* **34** (6), 065404.
- Van Gent, P., Michaelis, D., Van Oudheusden, B., Weiss, P. É., de Kat, R., Laskari, A., Jeon, Y. J., David, L., Schanz, D., Huhn, F. & others 2017a Comparative assessment of pressure field reconstructions from particle image velocimetry measurements and Lagrangian particle tracking. *Exp. Fluids* **58**, 1–23.
- Van Gent, P. L., Michaelis, D., Van Oudheusden, B. W., Weiss, P.-É., de Kat, R., Laskari, A., Jeon, Y. J., David, L., Schanz, D., Huhn, F., Gesemann, S., Novara, M., McPhaden, C., Neeteson, N. J., Rival, D. E., Schneiders, J. F. G. & Schrijer, F. F. J. 2017b Comparative assessment of pressure field reconstructions from particle image velocimetry measurements and Lagrangian particle tracking. *Exp. Fluids* **58**, 1–23.
- Venkatakrishnan, L. & Meier, G. E. A. 2004 Density measurements using the background oriented schlieren technique. *Exp. Fluids* **37**, 237–247.
- Voßkuhle, M., Pumir, A., Lévêque, E. & Wilkinson, M. 2014 Prevalence of the sling effect for enhancing collision rates in turbulent suspensions. *J. Fluid Mech.* **749**, 841–852.

- Wang, S., Teng, Y. & Perdikaris, P. 2021 Understanding and mitigating gradient flow pathologies in physics-informed neural networks. *SIAM J. Sci. Comput.* **43** (5), A3055–A3081.
- Wang, S., Yu, X. & Perdikaris, P. 2022 When and why PINNs fail to train: A neural tangent kernel perspective. *J. Comput. Phys.* **449**, 110768.
- Weiss, S., Schanz, D., Erdogan, A. O., Schröder, A. & Bosbach, J. 2023 Investigation of turbulent superstructures in Rayleigh–Bénard convection by Lagrangian particle tracking of fluorescent microspheres. *Exp. Fluids* **64** (4), 82.
- Wieneke, B. & Rockstroh, T. 2024 Lagrangian particle tracking in the presence of obstructing objects. *Meas. Sci. Technol.* **35** (5), 055303.
- Williams, O. J. H. 2014 Density Effects on Turbulent Boundary Layer Structure: From the Atmosphere to Hypersonic Flow. PhD thesis, Princeton University.
- Williams, O. J. H., Nguyen, T., Schreyer, A.-M. & Smits, A. J. 2015 Particle response analysis for particle image velocimetry in supersonic flows. *Phys. Fluids* **27** (7), 076101.
- Wissink, J. G. & Herlina, H. 2023 Surface-temperature-induced Marangoni effects on developing buoyancy-driven flow. *J. Fluid Mech.* **962**, A23.
- Wolf, C. C., Schwarz, C., Kaufmann, K., Gardner, A. D., Michaelis, D., Bosbach, J., Schanz, D. & Schröder, A. 2019 Experimental study of secondary vortex structures in a rotor wake. *Exp. Fluids* **60** (11), 175.
- Xiao, H. & Cinnella, P. 2019 Quantification of model uncertainty in RANS simulations: A review. *Prog. Aerosp. Sci.* **108**, 1–31.
- Zaki, T. A. 2025 Turbulence from an observer perspective. *Annu. Rev. Fluid Mech.* **57**.
- Zaki, T. A. & Wang, M. 2025 Data assimilation and flow estimation. In *Data Driven Analysis and Modeling of Turbulent Flows*, pp. 129–181. Elsevier.
- Zhang, W., Wang, Y. & Lee, S. J. 2008 Simultaneous PIV and PTV measurements of wind and sand particle velocities. *Exp. Fluids* **45**, 241–256.
- Zhou, K., Grauer, S. J., Schanz, D., Godbersen, P., Schröder, A., Rockstroh, T., Jeon, Y. J. & Wieneke, B. 2024 Benchmarking data assimilation algorithms for 3D Lagrangian particle tracking. In *21st International Symposium on Applications of Laser and Imaging Techniques to Fluid Mechanics*, p. 229.
- Zhou, K., Li, J., Hong, J. & Grauer, S. J. 2023 Stochastic particle advection velocimetry (SPAV): theory, simulations, and proof-of-concept experiments. *Meas. Sci. Technol.* **34** (6), 065302.